

Simplified multiphase lattice Boltzmann method for simulating multiphase flows with large density ratios and complex interfaces

Z. Chen,¹ C. Shu,^{1,*} D. Tan,¹ X. D. Niu,^{2,*} and Q. Z. Li²

¹*Department of Mechanical Engineering, National University of Singapore, 10 Kent Ridge Crescent, Singapore 119260, Singapore*

²*College of Engineering, Shantou University, 243 Daxue Road, Shantou, Guangdong 515063, China*



(Received 25 September 2018; published 26 December 2018)

In this paper, a simplified multiphase lattice Boltzmann method (SMLBM) is developed for modeling incompressible multiphase flows with large density ratios and complex interfaces. SMLBM is derived from reconstructing solutions to macroscopic equations recovered from the multiphase lattice Boltzmann model through Chapman-Enskog expansion analysis and resolved in a predictor-corrector step. The Cahn-Hilliard equation is utilized as the interface tracking algorithm, the solution of which is also reconstructed within the lattice Boltzmann framework. The resultant formulation of SMLBM reflects a direct update of macroscopic variables instead of distribution functions, which could remarkably save virtual memory and facilitate implementation of physical boundary conditions. Numerical tests also indicate that our scheme could effectively simulate challenging cases with large density ratios (up to 1000) and complex interfaces, and at high Reynolds numbers.

DOI: [10.1103/PhysRevE.98.063314](https://doi.org/10.1103/PhysRevE.98.063314)

I. INTRODUCTION

As a commonly encountered problem, incompressible flow with multiple components has always been an attractive topic in academics and engineering. Numerical simulation is a promising solution in this field due to its low cost, high efficiency, and flexibility. For the widely used Eulerian methods (e.g., finite difference method, finite volume method, etc.), extra algorithms are needed to track the evolution of interfaces. To resolve this issue, various numerical models, e.g., volume of fluid [1], level-set method [2], front tracking algorithm [3], diffuse interface method [4], etc., have been developed and applied in various multiphase flow problems in past decades.

Interests are growing in adopting lattice Boltzmann method (LBM) in multiphase simulations [5,6]. As a mesoscopic interpretation of fluid phenomena, LBM provides a distinct perspective for fluid behavior through simple streaming-collision processes [7]. It also preserves kinetic nature and facilitates implementation through an explicit evolution process, which are very valued characteristics in numerical simulations. Pioneering work in developing the multiphase lattice Boltzmann (LB) model was carried out by Gunstensen *et al.* [8], who developed the color-gradient model. Shan and Chen [9] then proposed another multiphase LB model which utilizes a newly defined interaction potential to consider nonlocal interactions among interface particles. Later, the free-energy approach was adopted by Swift *et al.* [10] in developing the multiphase LB model. After that, He *et al.* [11] introduced a novel incompressible transformation to the equilibrium distribution functions and proposed a double-distribution-functions (DDFs) model based on kinetic theory. This strategy was

further nurtured by various research groups [12,13], and was proven to be an effective solution to multiphase problems at high density ratios. Moreover, recent progresses in ternary lattice Boltzmann models [14–16] show that various multiphase LB models, including the DDFs model, can be extended to three-phase simulations by tuning the interface tracking strategy.

Despite the success of various multiphase LB models, it should be noted that they also inherit intrinsic drawbacks from the LBM. Representative limitations include high cost in virtual memories, inconvenient implementation of physical boundary conditions, and poor numerical stability at high Reynolds numbers [7,17–19]. Specifically, since LBM tracks the evolution of distribution functions, functional values along all lattice velocity directions must be stored. For the typical D2Q9 model, the DDFs model needs to store at least 18 variables on each mesh point, which would be a heavy burden to virtual memory. Meanwhile, physical boundary conditions related to the macroscopic variables have to be transformed into the boundary conditions for the distribution function to be implemented in LBM. Such transformation is tedious, and sometimes challenging when encountering curved boundaries. Moreover, the numerical stability of existing multiphase LB models is poor at high Reynolds numbers. The stability analysis in the single-phase scenario indicates that LBM is highly unstable when the relaxation parameter τ approaches 0.5 [20]. Although no analytical analysis has been performed in the multiphase scenario, the above conclusion is widely accepted and is also numerically validated in multiphase simulations [12].

Various attempts have been made in modifying collision models, which aim to enhance the performance of LBM in simulating multiphase flows with high density ratios or Reynolds numbers. Typical examples include the multiple relaxation time (MRT) based multiphase model [21,22] and

*Corresponding authors: mpeshuc@nus.edu.sg; xdnui@stu.edu.cn

the model developed from the entropic lattice Boltzmann method [23]. Numerical tests indicate that these models show much better numerical stability than the conventional multiphase lattice Boltzmann model at high Reynolds numbers.

A recent progress in the LBM community is the simplified lattice Boltzmann method (SLBM) [24,25]. This method is developed within the LB framework and can eliminate or alleviate drawbacks of previous LB models. SLBM is derived by reconstructing solutions to macroscopic equations recovered from the lattice Boltzmann equation (LBE) through Chapman-Enskog (C-E) expansion analysis and resolved in a predictor-corrector scheme. The resultant formulations reflect an explicit evolution of macroscopic variables instead of distribution functions, which reduces the memory cost and facilitates implementation of physical boundary conditions. Stability analysis could be performed on SLBM to prove that, under the incompressible limit, the scheme is stable in all wave numbers at high Reynolds numbers [25]. This is indeed an unprecedented characteristic among various LB models.

Given its good performance in single-phase modeling, we have good reason to expect that these merits could be inherited if SLBM is extended to the multiphase scenario. The purpose of the present paper is to follow the idea of SLBM to develop a simplified multiphase lattice Boltzmann method (SMLBM). The derivation will start from the macroscopic governing equations recovered from the multiphase lattice Boltzmann model through C-E analysis. By using lattice properties and relationships given in C-E analysis, flow variables could be updated by reconstructing solutions to the recovered macroscopic equations. The Cahn-Hilliard (C-H) equation is utilized as the interface tracking algorithm in our method, in which the order parameter is updated in a similar manner within the LB framework.

Various advantages could be achieved by adopting SMLBM in multiphase modeling. On one hand, since SMLBM is developed within the LB framework, it maintains intrinsic merits of multiphase LB models like kinetic nature, simplicity, and explicitness. On the other hand, by directly updating macroscopic variables instead of distribution functions, large amounts of virtual memory are saved, and physical boundary conditions could be directly implemented. The most appealing characteristic of SMLBM, which will be shown in our numerical examples, is that it is highly stable in problems with large density ratios and complex interfaces and at high Reynolds numbers. The possible reason is that SMLBM inherits the good stability feature of the reconstruction strategy of SLBM. These characteristics indicate that SMLBM is not only an alternative multiphase solution within the LB framework but also a promising tool for real engineering problems with large density ratios and at high Reynolds numbers.

The remaining parts of this paper are organized as follows. Section II provides theoretical foundations for the present method. Detailed derivations of formulations of SMLBM are presented in Sec. III. Comprehensive validations of SMLBM are performed in Sec. IV through a series of representative examples with large density ratios and complex interfaces, and at high Reynolds numbers. Conclusions are finally drawn in Sec. V.

II. GOVERNING EQUATIONS

A. Multiphase lattice Boltzmann model

In lattice Boltzmann method, the evolution of the flow field is accomplished by updating the density distribution functions. Unlike the single-phase scenario, discontinuity of density exists in flow fields with multiple components. To tackle the numerical challenges induced by density discontinuity, a novel incompressible transformation was introduced by He *et al.* [11], and the following multiphase lattice Boltzmann model could be developed [12,26]:

$$f_\alpha(\mathbf{r} + \mathbf{e}_\alpha \delta_t, t + \delta_t) = f_\alpha(\mathbf{r}, t) - \frac{f_\alpha(\mathbf{r}, t) - f_\alpha^{\text{eq}}(\mathbf{r}, t)}{\tau} + H_\alpha \quad (1)$$

where

$$H_\alpha = \left(1 - \frac{1}{2\tau}\right)(\mathbf{e}_\alpha - \mathbf{u}) \cdot [\Gamma_\alpha(\mathbf{u})(\mathbf{F}_s + \mathbf{G}) - (\Gamma_\alpha(\mathbf{u}) - \Gamma_\alpha(0))\nabla\psi(\rho)], \quad (2)$$

$$f_\alpha^{\text{eq}} = \rho c_s^2 \Gamma_\alpha(\mathbf{u}) + \psi(\rho) \Gamma_\alpha(0) \\ = \omega_\alpha \left[p + \rho c_s^2 \left(\frac{\mathbf{e}_\alpha \cdot \mathbf{u}}{c_s^2} + \frac{(\mathbf{e}_\alpha \cdot \mathbf{u})^2}{2c_s^4} - \frac{|\mathbf{u}|^2}{2c_s^2} \right) \right], \quad (3)$$

$$\Gamma_\alpha(\mathbf{u}) = \omega_\alpha \left[1 + \frac{\mathbf{e}_\alpha \cdot \mathbf{u}}{c_s^2} + \frac{(\mathbf{e}_\alpha \cdot \mathbf{u})^2}{2c_s^4} - \frac{|\mathbf{u}|^2}{2c_s^2} \right], \quad (4)$$

$$\psi(\rho) = p - \rho c_s^2. \quad (5)$$

Note that p , ρ , and \mathbf{u} denote the pressure, density, and velocity vector, respectively; f_α is the particle distribution function along the lattice velocity direction α and f_α^{eq} is its corresponding equilibrium distribution function; \mathbf{e}_α and ω_α are the lattice velocity vector and the weighting coefficient; ψ is the term emerged from incompressible transformation [11]; H_α represents the forcing term, in which \mathbf{F}_s and \mathbf{G} represent the surface tension force and the gravitational force, respectively; c_s represents the sound speed; τ is the single relaxation parameter which is related to the kinematic viscosity ν of fluid through

$$\nu = c_s^2 \delta_t (\tau - 0.5), \quad (6)$$

where δ_t is the time interval.

The above multiphase lattice Boltzmann model is associated with a specific lattice velocity model. One widely used lattice velocity model in two-dimensional problems is the D2Q9 model [27], in which the lattice velocity vectors, weighting coefficients, and sound speed are defined as

$$\mathbf{e}_\alpha = \begin{cases} 0 & \alpha = 0 \\ (\pm 1, 0), (0, \pm 1) & \alpha = 1, 2, 3, 4, \\ (\pm 1, \pm 1) & \alpha = 5, 6, 7, 8 \end{cases} \quad (7)$$

$$\omega_0 = \frac{4}{9}, \quad \omega_{1-4} = \frac{1}{9}, \quad \omega_{5-8} = \frac{1}{36}, \quad c_s = \frac{c}{\sqrt{3}}, \quad (8)$$

where $c = \delta_x / \delta_t$ is set to be 1, and δ_x is the lattice spacing.

B. Cahn-Hilliard equation within the lattice Boltzmann framework

The above formulations could resolve the pressure and the velocity of the flow field. An extra algorithm is required to update the discontinuous density field and identify the multiphase interfaces. The phase field method is a popular approach to fulfill that requirement. Typical mathematical models within this category include the Cahn-Hilliard equation, the Allen-Cahn equation, and their conservative forms [28–30]. In phase field method, the evolution is achieved by the Cahn-Hilliard equation in the following macroscopic form:

$$\frac{\partial C}{\partial t} + (\mathbf{u} \cdot \nabla)C = M \nabla^2 \mu_C \quad (9)$$

where C is the order parameter; M denotes the mobility; and μ_C is the chemical potential which could be expressed as

$$\mu_C = 2\beta C(C-1)(2C-1) - \kappa \nabla^2 C \quad (10)$$

where β and κ are two constants determined by the thickness of interface ξ and the surface tension coefficient σ through

$$\sigma = \sqrt{2\kappa\beta}/6, \quad (11)$$

$$\kappa = \beta\xi^2/8. \quad (12)$$

Within the Cahn-Hilliard model, the surface tension force can be evaluated by

$$\mathbf{F}_s = -C \nabla \mu_C. \quad (13)$$

The Cahn-Hilliard equation can be equally constructed within the lattice Boltzmann framework using distribution functions. Exploration was carried out by Zheng *et al.* [31] with further simplifications made by Huang *et al.* [32]. The evolution formulation reads

$$g_\alpha(\mathbf{r} + \mathbf{e}_\alpha \delta_t, t + \delta_t) = g_\alpha(\mathbf{r}, t) - \frac{g_\alpha(\mathbf{r}, t) - g_\alpha^{\text{eq}}(\mathbf{r}, t)}{\tau_C}, \quad (14)$$

where τ_C is the relaxation parameter; g_α is the distribution function of the order parameter with its equilibrium state expressed as

$$g_\alpha^{\text{eq}} = \begin{cases} C - \mu_C Q(1 - \omega_0)/c_s^2, & \alpha = 0 \\ \omega_\alpha(\mu_C Q + C \mathbf{e}_\alpha \cdot \mathbf{u})/c_s^2, & \alpha = 1-8 \end{cases}, \quad (15)$$

where Q is a diffusion parameter which is related to the mobility through

$$M = (\tau_C - 0.5)Q\delta_t. \quad (16)$$

C. Chapman-Enskog expansion analysis

The lattice Boltzmann method is constructed in the mesoscopic scale. Since the problem described is the same, it should be consistent with the macroscopic interpretation. The multiscale C-E expansion analysis plays an essential role in proving such consistency. In this section, the C-E analysis is performed on the multiphase lattice Boltzmann model and the Cahn-Hilliard equation within the lattice Boltzmann framework. The obtained macroscopic equations will be utilized to derive formulations of the SMLBM proposed in this paper.

Define the following:

$$f_\alpha = f_\alpha^{(0)} + \varepsilon f_\alpha^{(1)} + \varepsilon^2 f_\alpha^{(2)}, \quad \partial_t = \varepsilon \partial_{t_0} + \varepsilon^2 \partial_{t_1}, \\ \nabla = \varepsilon \nabla_1, \quad H_\alpha = \varepsilon H_\alpha^{(1)}. \quad (17)$$

Substituting Eq. (17) into Eq. (1) gives

$$\left(\varepsilon \frac{\partial}{\partial t_0} + \varepsilon^2 \frac{\partial}{\partial t_1} + \varepsilon \mathbf{e}_\alpha \cdot \nabla_1 \right) (f_\alpha^{(0)} + \varepsilon f_\alpha^{(1)} + \varepsilon^2 f_\alpha^{(2)}) \\ + \frac{\delta_t}{2} \left(\varepsilon \frac{\partial}{\partial t_0} + \varepsilon^2 \frac{\partial}{\partial t_1} + \varepsilon \mathbf{e}_\alpha \cdot \nabla_1 \right)^2 (f_\alpha^{(0)} + \varepsilon f_\alpha^{(1)} + \varepsilon^2 f_\alpha^{(2)}) \\ = -\frac{1}{\tau \delta_t} (f_\alpha^{(0)} + \varepsilon f_\alpha^{(1)} + \varepsilon^2 f_\alpha^{(2)} - f_\alpha^{\text{eq}}) + \left(1 - \frac{1}{2\tau} \right) \varepsilon H_\alpha^{(1)}. \quad (18)$$

From the above equation, the following relationships can be established in different scales:

$$\varepsilon^0 : f_\alpha^{(0)} = f_\alpha^{\text{eq}}, \quad (19)$$

$$\varepsilon^1 : \frac{\partial}{\partial t_0} f_\alpha^{(0)} + \mathbf{e}_\alpha \cdot \nabla_1 f_\alpha^{(0)} = -\frac{1}{\tau \delta_t} f_\alpha^{(1)} + H_\alpha^{(1)}, \quad (20)$$

$$\varepsilon^2 : \frac{\partial}{\partial t_1} f_\alpha^{(0)} + \frac{\partial}{\partial t_0} \left(1 - \frac{1}{2\tau} \right) f_\alpha^{(1)} + \mathbf{e}_\alpha \cdot \nabla_1 \left(1 - \frac{1}{2\tau} \right) f_\alpha^{(1)} \\ = -\frac{1}{\tau \delta_t} f_\alpha^{(2)} - \frac{\delta_t}{2} \left(\frac{\partial}{\partial t_0} + \mathbf{e}_\alpha \cdot \nabla_1 \right) H_\alpha^{(1)}, \quad (21)$$

and the following relationships are established [26]:

$$\sum_\alpha f_\alpha^{(1)} = \frac{1}{2} \mathbf{u} \cdot \nabla_1 \psi(\rho) \delta_t, \quad \sum_\alpha \mathbf{e}_\alpha f_\alpha^{(1)} = -\frac{c_s^2}{2} (\mathbf{F}_s + \mathbf{G})_1 \delta_t, \quad (22)$$

$$\sum_\alpha f_\alpha^{(2)} = \sum_\alpha \mathbf{e}_\alpha f_\alpha^{(2)} = 0, \quad (23)$$

$$\sum_\alpha H_\alpha = -\left(1 - \frac{1}{2\tau} \right) \mathbf{u} \cdot \nabla \psi(\rho),$$

$$\sum_\alpha \mathbf{e}_\alpha H_\alpha = \left(1 - \frac{1}{2\tau} \right) c_s^2 (\mathbf{F}_s + \mathbf{G}). \quad (24)$$

From Eq. (20), the nonequilibrium part is expressed as

$$\varepsilon f_\alpha^{(1)} = -\tau \delta_t D f_\alpha^{\text{eq}} + \tau \delta_t H_\alpha, \quad (25)$$

where the operator D represents $(\frac{\partial}{\partial t} + \mathbf{e}_\alpha \cdot \nabla)$.

Summation of the zeroth-order and the first-order moments of Eqs. (20) and (21), together with relationships in Eqs. (22)–(25), can recover the following macroscopic equations:

$$\frac{\partial p}{\partial t} + \nabla \cdot \sum_\alpha \mathbf{e}_\alpha f_\alpha^{\text{eq}} = \mathbf{u} \cdot \nabla \rho c_s^2, \quad (26)$$

$$\frac{\partial \rho \mathbf{u} c_s^2}{\partial t} + \nabla \cdot \sum_\alpha (\mathbf{e}_\alpha)_j (\mathbf{e}_\alpha)_k \left[f_\alpha^{\text{eq}} - \left(\tau - \frac{1}{2} \right) \delta_t D f_\alpha^{\text{eq}} \right] \\ + \nabla \cdot \tau \delta_t \sum_\alpha (\mathbf{e}_\alpha)_j (\mathbf{e}_\alpha)_k H_\alpha = c_s^2 (\mathbf{F}_s + \mathbf{G}). \quad (27)$$

Note that, with the relationships in Eqs. (22)–(25), one can derive the following formulations:

$$\sum_{\alpha} Df_{\alpha}^{\text{eq}} = -\mathbf{u} \cdot \nabla \psi(\rho), \quad (28)$$

$$\sum_{\alpha} \mathbf{e}_{\alpha} Df_{\alpha}^{\text{eq}} = c_s^2 (\mathbf{F}_s + \mathbf{G}). \quad (29)$$

Through similar process, the following macroscopic equation for the order parameter can be recovered:

$$\frac{\partial C}{\partial t} + \nabla \cdot \sum_{\alpha} \mathbf{e}_{\alpha} g_{\alpha}^{\text{eq}} + \nabla \cdot \left(\frac{1}{2} - \tau_c \right) \delta_t \sum_{\alpha} \mathbf{e}_{\alpha} Dg_{\alpha}^{\text{eq}} = 0. \quad (30)$$

Details for deriving Eqs. (26), (27), and (30) will be attached in the Appendix.

III. SIMPLIFIED MULTIPHASE LATTICE BOLTZMANN METHOD

A. Reconstruction of flow variables

The essence of simplified lattice Boltzmann method is to reconstruct solutions to macroscopic equations recovered from the lattice Boltzmann equation. Therefore, in this section, we follow a similar strategy to reconstruct solutions to Eqs. (26) and (27). The reconstruction is carried out in a

predictor-corrector strategy, which is based on the fractional step technique [33]. By splitting the original equations into two parts and resolving them separately, enriched flexibility can be achieved in constructing numerical schemes.

In the predictor step, solutions to the following macroscopic equations will be reconstructed:

$$\frac{\partial p}{\partial t} + \nabla \cdot \sum_{\alpha} \mathbf{e}_{\alpha} f_{\alpha}^{\text{eq}}(\mathbf{r}, t) - \mathbf{u} \cdot \nabla \rho c_s^2 = 0, \quad (31)$$

$$\frac{\partial \rho \mathbf{u} c_s^2}{\partial t} + \nabla \cdot \sum_{\alpha} (\mathbf{e}_{\alpha})_{\beta} (\mathbf{e}_{\alpha})_{\gamma} \left[f_{\alpha}^{\text{eq}} - \frac{\delta_t}{2} Df_{\alpha}^{\text{eq}} \right] = 0. \quad (32)$$

To do that, intermediate flow variables are estimated as

$$p^* = \sum_{\alpha} f_{\alpha}^{\text{eq-m}}(\mathbf{r} - \mathbf{e}_{\alpha} \delta_t, t - \delta_t), \quad (33)$$

$$\rho^* \mathbf{u}^* c_s^2 = \sum_{\alpha} \mathbf{e}_{\alpha} f_{\alpha}^{\text{eq}}(\mathbf{r} - \mathbf{e}_{\alpha} \delta_t, t - \delta_t), \quad (34)$$

where the superscript “eq_m” represents the equilibrium distribution function computed from the density on the central mesh point and other flow variables on the streaming nodes. The derivation starts from Taylor series expansion of equilibrium distribution functions

$$f_{\alpha}^{\text{eq-m}}(\mathbf{r} - \mathbf{e}_{\alpha} \delta_t, t - \delta_t) = f_{\alpha}^{\text{eq}}(\mathbf{r} - \mathbf{e}_{\alpha} \delta_t, t - \delta_t) + (\Gamma_{\alpha}(\mathbf{u}) - \Gamma_{\alpha}(0)) \mathbf{e}_{\alpha} \delta_t \cdot \nabla \rho c_s^2 + O(\delta_t^2), \quad (35)$$

$$f_{\alpha}^{\text{eq}}(\mathbf{r} - \mathbf{e}_{\alpha} \delta_t, t - \delta_t) = f_{\alpha}^{\text{eq}}(\mathbf{r}, t) - \delta_t Df_{\alpha}^{\text{eq}}(\mathbf{r}, t) + \frac{\delta_t^2}{2} D^2 f_{\alpha}^{\text{eq}}(\mathbf{r}, t) + O(\delta_t^3). \quad (36)$$

Under the incompressible limit, we can derive the following relationship:

$$\sum_{\alpha} (\Gamma_{\alpha}(\mathbf{u}) - \Gamma_{\alpha}(0)) (\mathbf{e}_{\alpha} \cdot \nabla \rho c_s^2) = c_s^2 \mathbf{u} \cdot \nabla \rho. \quad (37)$$

Substituting Eqs. (35)–(37) into Eqs. (33) and (34) gives

$$\begin{aligned} p^* &= \sum_{\alpha} \left[f_{\alpha}^{\text{eq}}(\mathbf{r} - \mathbf{e}_{\alpha} \delta_t, t - \delta_t) + (\Gamma_{\alpha}(\mathbf{u}) - \Gamma_{\alpha}(0)) \mathbf{e}_{\alpha} \delta_t \cdot \nabla \rho c_s^2 + O(\delta_t^2) \right] \\ &= \sum_{\alpha} f_{\alpha}^{\text{eq}}(\mathbf{r}, t) - \delta_t \sum_{\alpha} Df_{\alpha}^{\text{eq}}(\mathbf{r}, t) + \delta_t \sum_{\alpha} (\Gamma_{\alpha}(\mathbf{u}) - \Gamma_{\alpha}(0)) \mathbf{e}_{\alpha} \cdot \nabla \rho c_s^2 + O(\delta_t^2) \\ &= p(\mathbf{r}, t) - \delta_t \left[\frac{\partial p}{\partial t} + \nabla \cdot \sum_{\alpha} \mathbf{e}_{\alpha} f_{\alpha}^{\text{eq}}(\mathbf{r}, t) - \mathbf{u} \cdot \nabla \rho c_s^2 + O(\delta_t) \right], \end{aligned} \quad (38)$$

$$\begin{aligned} \rho^* \mathbf{u}^* c_s^2 &= \sum_{\alpha} \mathbf{e}_{\alpha} \left[f_{\alpha}^{\text{eq}}(\mathbf{r}, t) - \delta_t Df_{\alpha}^{\text{eq}}(\mathbf{r}, t) + \frac{\delta_t^2}{2} D^2 f_{\alpha}^{\text{eq}}(\mathbf{r}, t) + O(\delta_t^3) \right] \\ &= \rho(\mathbf{r}, t) \mathbf{u}(\mathbf{r}, t) c_s^2 - \delta_t \left[\frac{\partial \rho \mathbf{u} c_s^2}{\partial t} + \nabla \cdot \sum_{\alpha} (\mathbf{e}_{\alpha})_{\beta} (\mathbf{e}_{\alpha})_{\gamma} f_{\alpha}^{\text{eq}} - \frac{\delta_t}{2} \sum_{\alpha} \mathbf{e}_{\alpha} D^2 f_{\alpha}^{\text{eq}}(\mathbf{r}, t) + O(\delta_t^2) \right]. \end{aligned} \quad (39)$$

Omitting minor terms, the recovered macroscopic equations in the predictor step, i.e., Eqs. (31) and (32), are recovered. As can be seen, the reconstruction of the continuity equation is in the first order of accuracy. Given the fact that the pressure field is relatively smooth, such approximation is acceptable in numerical simulation. The recovered continuity equation in the predictor step is identical to Eq. (26), while the corrector step for the velocity is still necessary to achieve the accurate momentum equation.

In the corrector step, the target macroscopic equations are

$$\frac{\partial p}{\partial t} = 0, \quad (40)$$

$$\frac{\partial \rho \mathbf{u} c_s^2}{\partial t} - \nabla \cdot (\tau - 1) \sum_{\alpha} (\mathbf{e}_{\alpha})_{\beta} (\mathbf{e}_{\alpha})_{\gamma} \delta_t Df_{\alpha}^{\text{eq}} + \nabla \cdot \tau \delta_t \sum_{\alpha} (\mathbf{e}_{\alpha})_j (\mathbf{e}_{\alpha})_k H_{\alpha} = c_s^2 (\mathbf{F}_s + \mathbf{G}), \quad (41)$$

and the formulations of reconstruction are tailored as

$$p^{n+1} = p^*, \quad (42)$$

$$\begin{aligned} \rho^{n+1} \mathbf{u}^{n+1} c_s^2 &= \rho^* \mathbf{u}^* c_s^2 + \sum_{\alpha} \mathbf{e}_{\alpha} \left[f_{\alpha}^{\sim} \left(\mathbf{r} + \frac{1}{2} \mathbf{e}_{\alpha} \delta_t, t - \frac{1}{2} \delta_t \right) - f_{\alpha}^{\sim} \left(\mathbf{r} - \frac{1}{2} \mathbf{e}_{\alpha} \delta_t, t - \frac{1}{2} \delta_t \right) \right] \\ &\quad - \frac{\delta_t}{2} \sum_{\alpha} \mathbf{e}_{\alpha} \left[H_{\alpha}^{\sim} \left(\mathbf{r} + \mathbf{e}_{\alpha} \delta_t, t - \frac{1}{2} \delta_t \right) - H_{\alpha}^{\sim} \left(\mathbf{r} - \mathbf{e}_{\alpha} \delta_t, t - \frac{1}{2} \delta_t \right) \right] + c_s^2 (\mathbf{F}_s + \mathbf{G}) \delta_t \end{aligned} \quad (43)$$

where

$$f_{\alpha}^{\sim} \left(\mathbf{r} + \frac{1}{2} \mathbf{e}_{\alpha} \delta_t, t - \frac{1}{2} \delta_t \right) = (\tau(\mathbf{r} + \frac{1}{2} \mathbf{e}_{\alpha} \delta_t, t - \frac{1}{2} \delta_t) - 1) [f_{\alpha}^{\text{eq}}(\mathbf{r} + \mathbf{e}_{\alpha} \delta_t, t) - f_{\alpha}^{\text{eq}}(\mathbf{r}, t - \delta_t)], \quad (44)$$

$$f_{\alpha}^{\sim} \left(\mathbf{r} - \frac{1}{2} \mathbf{e}_{\alpha} \delta_t, t - \frac{1}{2} \delta_t \right) = (\tau(\mathbf{r} - \frac{1}{2} \mathbf{e}_{\alpha} \delta_t, t - \frac{1}{2} \delta_t) - 1) [f_{\alpha}^{\text{eq}}(\mathbf{r}, t) - f_{\alpha}^{\text{eq}}(\mathbf{r} - \mathbf{e}_{\alpha} \delta_t, t - \delta_t)], \quad (45)$$

$$H_{\alpha}^{\sim} = \tau H_{\alpha}. \quad (46)$$

The above formulations require physical quantities at the time level of t . As per Shu *et al.*'s suggestion [34], intermediate flow variables obtained in the predictor step are utilized here as the flow variables at the time level of t .

Equation (42) recovers Eq. (40) precisely. Adopting Taylor series expansion analysis gives the following relationships:

$$\begin{aligned} f_{\alpha}^{\sim}(\mathbf{r} \pm \frac{1}{2} \mathbf{e}_{\alpha} \delta_t, t - \frac{1}{2} \delta_t) &= (\tau(\mathbf{r} \pm \frac{1}{2} \mathbf{e}_{\alpha} \delta_t, t - \frac{1}{2} \delta_t) - 1) \delta_t D f_{\alpha}^{\text{eq}}(\mathbf{r} \pm \frac{1}{2} \mathbf{e}_{\alpha} \delta_t, t - \frac{1}{2} \delta_t) + O(\delta_t^3) \\ &= (\tau(\mathbf{r}, t - \frac{1}{2} \delta_t) - 1) \delta_t D f_{\alpha}^{\text{eq}}(\mathbf{r}, t - \frac{1}{2} \delta_t) \pm \frac{1}{2} \mathbf{e}_{\alpha} \delta_t^2 \cdot \nabla [(\tau(\mathbf{r}, t - \frac{1}{2} \delta_t) - 1) D f_{\alpha}^{\text{eq}}(\mathbf{r}, t - \frac{1}{2} \delta_t)] + O(\delta_t^3), \end{aligned} \quad (47)$$

$$\delta_t H_{\alpha}^{\sim}(\mathbf{r} \pm \mathbf{e}_{\alpha} \delta_t, t - \frac{1}{2} \delta_t) = \delta_t \tau(\mathbf{r}, t - \frac{1}{2} \delta_t) H_{\alpha}(\mathbf{r}, t - \frac{1}{2} \delta_t) \pm \mathbf{e}_{\alpha} \delta_t^2 \cdot \nabla [\tau(\mathbf{r}, t - \frac{1}{2} \delta_t) H_{\alpha}(\mathbf{r}, t - \frac{1}{2} \delta_t)] + O(\delta_t^3). \quad (48)$$

Here, the spatial accuracy of the approximated terms is in the third order $O(\delta_t^3)$. The marching in time levels would yield a division by δ_t , which ensures the consistency with the desired second order of accuracy in space. Meanwhile, the time levels of all approximated terms are shifted by half a time step, which would facilitate the construction of the central difference scheme in time marching and ensure the second order of accuracy in time. Substituting Eqs. (47) and (48) into Eq. (43) leads to

$$\frac{\rho^{n+1} \mathbf{u}^{n+1} c_s^2 - \rho^* \mathbf{u}^* c_s^2}{\delta_t} = \left[\nabla \cdot (\tau - 1) \sum_{\alpha} (\mathbf{e}_{\alpha})_{\beta} (\mathbf{e}_{\alpha})_{\gamma} D f_{\alpha}^{\text{eq}} - \nabla \cdot \tau \delta_t \sum_{\alpha} (\mathbf{e}_{\alpha})_{\beta} (\mathbf{e}_{\alpha})_{\gamma} H_{\alpha} + c_s^2 (\mathbf{F}_s + \mathbf{G}) \right]_{\mathbf{r}, t - 0.5 \delta_t} + O(\delta_t^2). \quad (49)$$

Given the consistency between Eqs. (49) and (41) in the second order of accuracy, it is proven that Eq. (43) could recover the solution to Eq. (41) with the second order of accuracy in both time and space.

B. Reconstruction of the order parameter

The reconstruction of the order parameter C follows a similar pattern as for the reconstruction of flow variables. The predictor-corrector scheme is adopted here to reconstruct the solution to Eq. (30). In the predictor step, the macroscopic governing equation reads

$$\frac{\partial C}{\partial t} + \nabla \cdot \sum_{\alpha} \mathbf{e}_{\alpha} g_{\alpha}^{\text{eq}} - \nabla \cdot \frac{1}{2} \delta_t \sum_{\alpha} \mathbf{e}_{\alpha} D g_{\alpha}^{\text{eq}} = 0. \quad (50)$$

In the present method, the intermediate order parameter in this step is estimated as

$$C^* = \sum_{\alpha} g_{\alpha}^{\text{eq}}(\mathbf{r} - \mathbf{e}_{\alpha} \delta_t, t - \delta_t). \quad (51)$$

Taylor series expansion of the equilibrium distribution would derive the above equation into

$$\begin{aligned} C^* &= \sum_{\alpha} \left[g_{\alpha}^{\text{eq}}(\mathbf{r}, t) - \delta_t D g_{\alpha}^{\text{eq}}(\mathbf{r}, t) + \frac{\delta_t^2}{2} D^2 g_{\alpha}^{\text{eq}}(\mathbf{r}, t) + O(\delta_t^3) \right] \\ &= C(\mathbf{r}, t) - \delta_t \left[\frac{\partial C}{\partial t} + \nabla \cdot \sum_{\alpha} \mathbf{e}_{\alpha} g_{\alpha}^{\text{eq}} - \frac{\delta_t}{2} \nabla \cdot \sum_{\alpha} \mathbf{e}_{\alpha} D g_{\alpha}^{\text{eq}}(\mathbf{r}, t) + O(\delta_t^2) \right]. \end{aligned} \quad (52)$$

Therefore, it is proven that the proposed formulation (51) could recover the macroscopic equation (50) with the second order of accuracy.

In the corrector step, the macroscopic governing equation to be recovered is

$$\frac{\partial C}{\partial t} - \nabla \cdot (\tau_C - 1) \delta_t \sum_{\alpha} \mathbf{e}_{\alpha} D g_{\alpha}^{\text{eq}} = 0, \quad (53)$$

and the following reconstruction formulation is proposed:

$$C^{n+1} = C^* + \sum_{\alpha} (\tau_C - 1) \left[g_{\alpha}^{\sim} \left(\mathbf{r} + \frac{1}{2} \mathbf{e}_{\alpha} \delta_t, t - \frac{1}{2} \delta_t \right) - g_{\alpha}^{\sim} \left(\mathbf{r} - \frac{1}{2} \mathbf{e}_{\alpha} \delta_t, t - \frac{1}{2} \delta_t \right) \right] \quad (54)$$

where

$$g_{\alpha}^{\sim} \left(\mathbf{r} + \frac{1}{2} \mathbf{e}_{\alpha} \delta_t, t - \frac{1}{2} \delta_t \right) = g_{\alpha}^{\text{eq}}(\mathbf{r} + \mathbf{e}_{\alpha} \delta_t, t) - g_{\alpha}^{\text{eq}}(\mathbf{r}, t - \delta_t), \quad (55)$$

$$g_{\alpha}^{\sim} \left(\mathbf{r} - \frac{1}{2} \mathbf{e}_{\alpha} \delta_t, t - \frac{1}{2} \delta_t \right) = g_{\alpha}^{\text{eq}}(\mathbf{r}, t) - g_{\alpha}^{\text{eq}}(\mathbf{r} - \mathbf{e}_{\alpha} \delta_t, t - \delta_t). \quad (56)$$

Similar to the treatment in reconstructing flow variables, the intermediate order parameter is utilized here as the quantity in the time level of t .

The proof of the formulation in the corrector step starts from Taylor series analysis of g_{α}^{\sim} :

$$g_{\alpha}^{\sim} \left(\mathbf{r} \pm \frac{1}{2} \mathbf{e}_{\alpha} \delta_t, t - \frac{1}{2} \delta_t \right) = \delta_t D g_{\alpha}^{\text{eq}} \left(\mathbf{r} \pm \frac{1}{2} \mathbf{e}_{\alpha} \delta_t, t - \frac{1}{2} \delta_t \right) + O(\delta_t^3) = \delta_t D g_{\alpha}^{\text{eq}}(\mathbf{r}, t - \frac{1}{2} \delta_t) \pm \frac{1}{2} \mathbf{e}_{\alpha} \delta_t^2 \cdot \nabla D g_{\alpha}^{\text{eq}}(\mathbf{r}, t - \frac{1}{2} \delta_t) + O(\delta_t^3). \quad (57)$$

Substituting Eq. (57) into Eq. (54) and performing further manipulations yields

$$\frac{C^{n+1} - C^*}{\delta_t} = \left[\nabla \cdot \sum_{\alpha} (\tau_C - 1) \mathbf{e}_{\alpha} \delta_t D g_{\alpha}^{\text{eq}} \right]_{\mathbf{r}, t - 0.5 \delta_t} + O(\delta_t^2). \quad (58)$$

As can be seen, Eq. (58) is a discretized form of Eq. (50) with the second order of accuracy. Therefore, the proposed formulation (54) could reconstruct the solution to Eq. (53) with the second order of accuracy in both space and time.

C. Formulations of SMLBM

For the ease of application, formulations of SMLBM are summarized as follows.

Predictor step:

$$p^* = \sum_{\alpha} f_{\alpha}^{\text{eq-m}}(\mathbf{r} - \mathbf{e}_{\alpha} \delta_t, t - \delta_t), \quad (59)$$

$$\rho^* \mathbf{u}^* c_s^2 = \sum_{\alpha} \mathbf{e}_{\alpha} f_{\alpha}^{\text{eq}}(\mathbf{r} - \mathbf{e}_{\alpha} \delta_t, t - \delta_t), \quad (60)$$

$$C^* = \sum_{\alpha} g_{\alpha}^{\text{eq}}(\mathbf{r} - \mathbf{e}_{\alpha} \delta_t, t - \delta_t). \quad (61)$$

Corrector step:

$$p^{n+1} = p^*, \quad (62)$$

$$\begin{aligned} \rho^{n+1} \mathbf{u}^{n+1} c_s^2 &= \rho^* \mathbf{u}^* c_s^2 + \sum_{\alpha} \mathbf{e}_{\alpha} \left[f_{\alpha}^{\sim} \left(\mathbf{r} + \frac{1}{2} \mathbf{e}_{\alpha} \delta_t, t - \frac{1}{2} \delta_t \right) - f_{\alpha}^{\sim} \left(\mathbf{r} - \frac{1}{2} \mathbf{e}_{\alpha} \delta_t, t - \frac{1}{2} \delta_t \right) \right] \\ &\quad - \frac{\delta_t}{2} \sum_{\alpha} \mathbf{e}_{\alpha} \left[H_{\alpha}^{\sim} \left(\mathbf{r} + \mathbf{e}_{\alpha} \delta_t, t - \frac{1}{2} \delta_t \right) - H_{\alpha}^{\sim} \left(\mathbf{r} - \mathbf{e}_{\alpha} \delta_t, t - \frac{1}{2} \delta_t \right) \right] + c_s^2 (\mathbf{F}_s + \mathbf{G}) \delta_t, \end{aligned} \quad (63)$$

$$C^{n+1} = C^* + \sum_{\alpha} (\tau_C - 1) \left[g_{\alpha}^{\sim} \left(\mathbf{r} + \frac{1}{2} \mathbf{e}_{\alpha} \delta_t, t - \frac{1}{2} \delta_t \right) - g_{\alpha}^{\sim} \left(\mathbf{r} - \frac{1}{2} \mathbf{e}_{\alpha} \delta_t, t - \frac{1}{2} \delta_t \right) \right] \quad (64)$$

where

$$f_{\alpha}^{\sim} \left(\mathbf{r} + \frac{1}{2} \mathbf{e}_{\alpha} \delta_t, t - \frac{1}{2} \delta_t \right) = (\tau(\mathbf{r} + \frac{1}{2} \mathbf{e}_{\alpha} \delta_t, t - \frac{1}{2} \delta_t) - 1) [f_{\alpha}^{\text{eq}}(\mathbf{r} + \mathbf{e}_{\alpha} \delta_t, t) - f_{\alpha}^{\text{eq}}(\mathbf{r}, t - \delta_t)], \quad (65)$$

$$f_{\alpha}^{\sim} \left(\mathbf{r} - \frac{1}{2} \mathbf{e}_{\alpha} \delta_t, t - \frac{1}{2} \delta_t \right) = (\tau(\mathbf{r} - \frac{1}{2} \mathbf{e}_{\alpha} \delta_t, t - \frac{1}{2} \delta_t) - 1) [f_{\alpha}^{\text{eq}}(\mathbf{r}, t) - f_{\alpha}^{\text{eq}}(\mathbf{r} - \mathbf{e}_{\alpha} \delta_t, t - \delta_t)], \quad (66)$$

$$H_\alpha^\sim = \tau H_\alpha, \quad (67)$$

$$g_\alpha^\sim(\mathbf{r} + \frac{1}{2}\mathbf{e}_\alpha\delta_t, t - \frac{1}{2}\delta) = g_\alpha^{\text{eq}}(\mathbf{r} + \mathbf{e}_\alpha\delta_t, t) - g_\alpha^{\text{eq}}(\mathbf{r}, t - \delta_t), \quad (68)$$

$$g_\alpha^\sim(\mathbf{r} - \frac{1}{2}\mathbf{e}_\alpha\delta_t, t - \frac{1}{2}\delta) = g_\alpha^{\text{eq}}(\mathbf{r}, t) - g_\alpha^{\text{eq}}(\mathbf{r} - \mathbf{e}_\alpha\delta_t, t - \delta_t). \quad (69)$$

Note that the intermediate properties obtained in the predictor step are utilized to evaluate equilibrium distribution functions at the time level of t ; ρ^* and ρ^{n+1} are calculated from C^* and C^{n+1} , respectively, with the following relationship:

$$\rho = \rho_d C + \rho_l (1 - C), \quad (70)$$

where subscripts d and l denote the denser and the lighter fluids, respectively. Note that the local viscosity μ on the mesh point is also evaluated by the linear interpolation with the order parameter.

As can be seen in the above formulations, although SMLBM is developed within the lattice Boltzmann framework, the primary variables in SMLBM are macroscopic variables instead of distribution functions. Various merits can then be expected. On one hand, SMLBM inherits the essence of the lattice Boltzmann method, which includes kinetic nature, simplicity, and explicitness. On the other hand, the direct evolution of macroscopic variables in SMLBM not only reduces cost in virtual memory but also facilitates implementation of physical boundary conditions. Specifically, when using the D2Q9 lattice velocity model, the conventional DDFs model would store 18 variables at each mesh point. The present SMLBM only needs to store the information of the density (order parameter), pressure, and velocity vector at each grid point. Even if storing these variables in two time levels, the present method would still lead to a theoretical reduction rate of more than 50% in memory cost. Of course, the practical reduction rate depends on the tricks adopted in programming, which is usually a compromise between numerical efficiency and memory cost. Since the equilibrium distribution functions need to be computed for an extra time in the corrector step, the present model may consume more computational time if compared with conventional DDFs models with the Bhatnagar-Gross-Krook collision operator. In terms of the boundary condition, no tedious transformation from physical boundary conditions into the condition of distribution functions is required, which facilitates the implementation. Another intriguing characteristic of SMLBM, which will be shown in some challenging numerical examples, is its good numerical stability. It could effectively model multiphase flows with large density ratios and complex interfaces, and at high Reynolds and Weber numbers.

D. Implementation of boundary conditions

As discussed above, the present SMLBM reflects an evolution of macroscopic variables in formulation. Therefore, physical boundary conditions can be directly implemented here without tedious transformation as required in conventional lattice Boltzmann method. Specifically, when implementing Dirichlet boundary conditions, boundary values of macroscopic variables are directly assigned to the boundary mesh points. When encountering Neumann boundary conditions,

information on several layers of inner meshes is utilized to determine values on the boundary mesh points with desired order of accuracy. In the present paper, two layers of inner meshes are utilized to ensure the second order of accuracy in space.

E. Computational sequence

The computational sequence of simplified multiphase lattice Boltzmann method can be summarized as follows.

- (1) Specify the streaming distance δ_x ($\delta_x = \delta_t$). Determine the relaxation parameter τ .
- (2) Predictor step. Use Eqs. (59)–(61) to evaluate intermediate physical properties p^* , ρ^* , \mathbf{u}^* and C^* .
- (3) Implement appropriate boundary conditions for the intermediate physical properties.
- (4) Corrector step. Update the macroscopic variables through Eqs. (62)–(64).
- (5) Implement appropriate boundary conditions for the macroscopic variables. The boundary conditions implemented here are essentially the same as those imposed in step (3).
- (6) Repeat steps (2)–(5) until the computation is converged or prescribed maximum iteration step is reached.

IV. NUMERICAL EXAMPLES

Five numerical examples, including the Laplace law, two merging bubbles, Rayleigh-Taylor (R-T) instability, bubble rising, and a droplet splashing on a thin film, are provided in this section to comprehensively evaluate the accuracy and robustness of the proposed SMLBM. It is noteworthy that the interface thickness ξ , which aims to ensure smooth transition of densities over the interface, varies from case to case. The value of ξ only affects the sharpness of the interface and does not influence the accuracy of computation. In our practice as well as previous reports in literature, a thicker interface is required in cases with higher density ratios.

A. Laplace's law

In this subsection, the benchmark test of Laplace's law is first performed to validate the implementation of surface tension force. The physical configuration of the problem is a static bubble immersed in another fluid with an analytically estimated pressure difference of $\Delta p = \sigma/R$, where R is the radius of the immersed bubble. The computational domain in our simulation is 201×201 , with periodic boundary conditions implemented on all boundaries. The density ratio is set as 100, and the relaxation parameter of $\tau = 0.8$ is used. Simulations are carried out at different surface tension coefficients and radii, and the computational results are presented in Fig. 1. It is observed that the numerical results are consistent with the

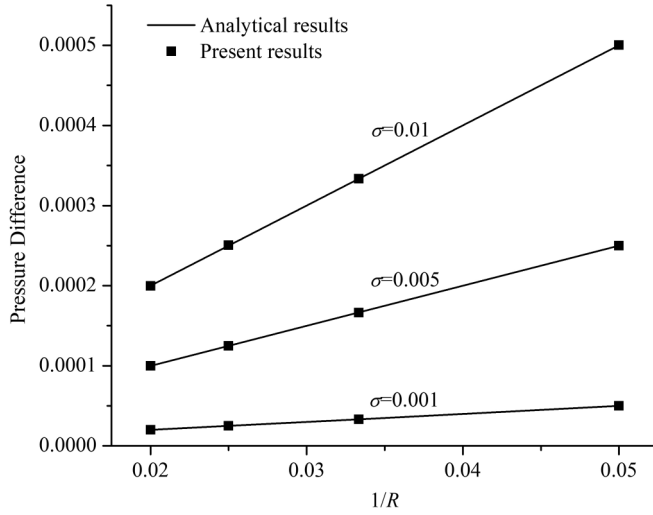


FIG. 1. Validation of Laplace's law.

analytical results with appealing accuracy, which validates the correct implementation of surface tension in our model.

Contours of the horizontal velocity at different density ratios and surface tension coefficients are presented in Fig. 2, in which the radius of the bubble is set to be 30. It is observed that increasing the surface tension force yields growth of the spurious current. In all cases, the magnitude of the spurious current is below the order of 10^{-5} , which demonstrates the low numerical noises of the proposed method.

B. Two merging bubbles

The example of two merging bubbles involves more complex interfacial changes and is simulated in this subsection for further validation of the proposed method. The physical configuration of this problem is two bubbles with partially overlapped interfaces. The merging of these two bubbles occurs due to the surface tension effect. The oscillations are then gradually diffused by the viscous effect, and eventually one single static bubble will form [31]. The computational setup in our simulation is a domain with the size of $[0, 240] \times [0, 200]$ with periodic boundary conditions implemented on all boundaries. Two bubbles with identical radius of $r = 25$ are initially placed at $(92, 100)$ and $(148, 100)$. The interface thickness is set as $\xi = 4$ to ensure the slight overlap of the diffuse interface which could trigger the merging process. Other flow parameters used in our simulation are $\rho_d/\rho_l = 100$, $\nu_d = \nu_l = 0.02$, $\tau_C = 1.2$, and $\sigma = 0.001$.

We first set the diffusion parameter Q as 1.0, which corresponds to the mobility of $M = 0.7$. The evolution of the interface in the merging process is presented in Fig. 3. As time marches, two bubbles gradually merge together; after a series of oscillations, the merged bubble forms a static shape of a perfect circle. The converged computational result is then presented and compared with the analytical solution in Fig. 4 for illustration of mass conservation. The analytical solution is given by $R_m = \sqrt{2}R_0$, where R_0 and R_m denote radii of the initial bubble and the merged bubble, respectively. The comparison reveals a relative error of 1.39% between the present result and the analytical solution, which validates the accuracy of the present method and its robustness in terms of

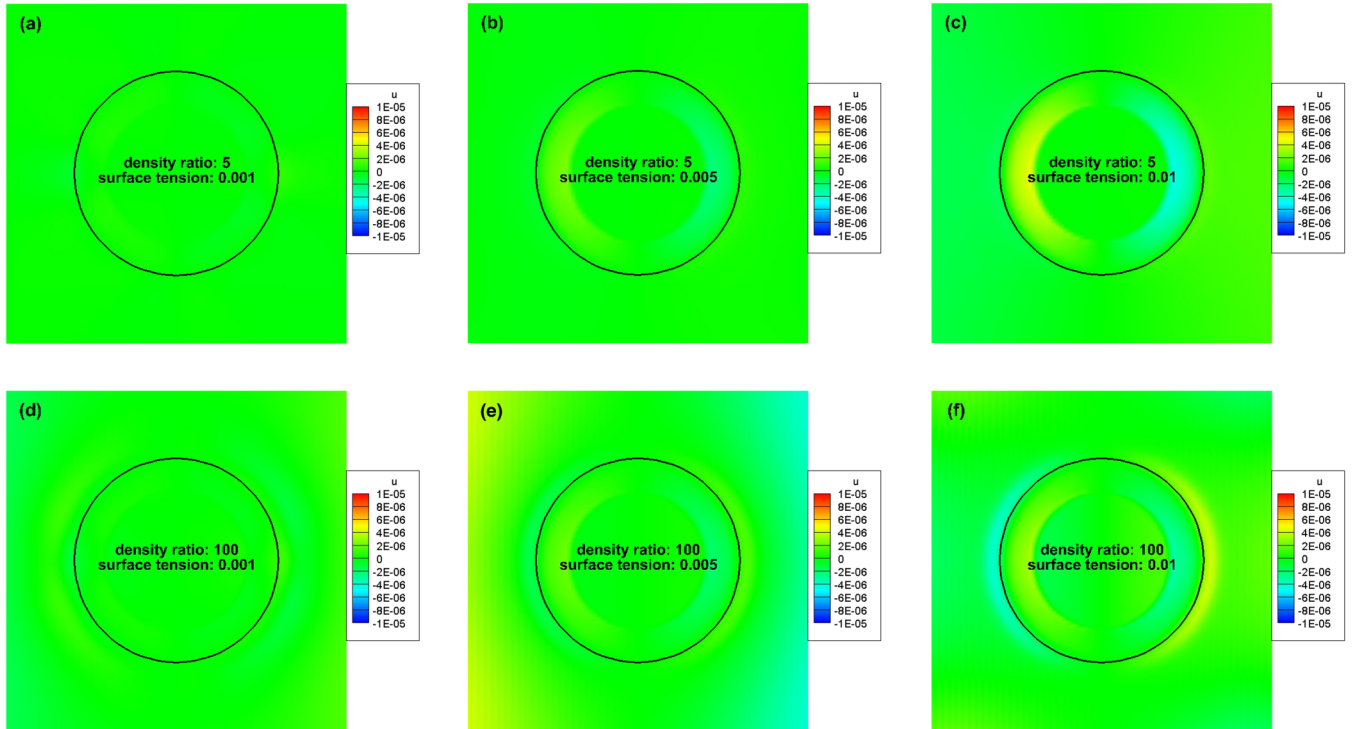


FIG. 2. Contours of horizontal velocity for the tests of Laplace's law. Black solid lines represent the interfacial positions.

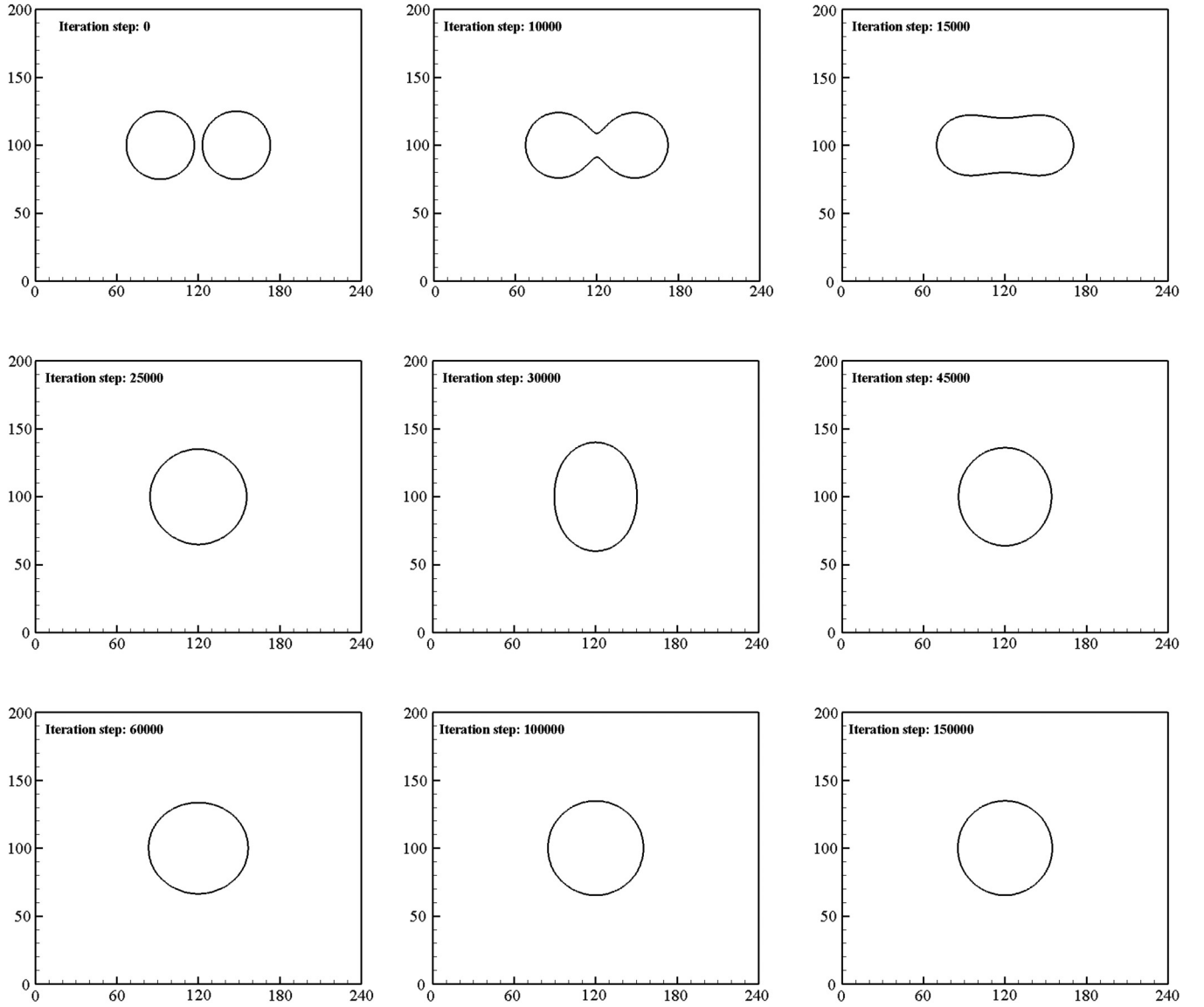


FIG. 3. Interface evolution of two merging bubbles.

mass conservation. Moreover, we could expect that, by replacing the Cahn-Hilliard equation with the conservative Allen-Cahn equation in updating interfacial motions [28,29,35], the performance of mass conservation would be further improved.

It is also known that the mobility of the Cahn-Hilliard model can significantly affect the coalescence process. To reveal that effect, comparative studies are carried out with three different values of diffusion parameters, i.e., $Q = 0.1, 1.0$, and 10.0 (respectively corresponding to $M = 0.07, 0.7$, and 7.0). Evolutions of the interfacial positions are presented in Fig. 5. It can be seen that a larger diffusion parameter would stimulate the coalescence process in the initial stage. Such stimulation can be explained by the higher artificial viscous effect brought about by the larger diffusion parameter. In the meantime, it was found that variation of diffusion parameters does not alter the final result of the merging process into one bubble, but will pose effects on the radius of the merged bubble. Due to the larger diffusion effect with

the larger diffusion parameter, the merged bubble seems to be more diffused, which is reflected by the reduction in radius.

C. Rayleigh-Taylor instability

In this subsection, the R-T instability, which is an unsteady problem with large deformation of interfaces, is simulated using the proposed method. The initial setup of R-T instability is a two-phase system with the denser fluid of density ρ_d placed on the lighter fluid with density ρ_l , and the instability is initiated by prescribed perturbation on the interface. In our simulation, a uniform mesh size of 201×801 is utilized to discretize the computational domain of $L \times 4L$. Periodic boundary conditions are implemented on the left and the right boundaries, while the top and the bottom walls satisfy no-slip boundary conditions. The initial interface between the two fluids is described as $y = 2L + 0.1L\cos(2\pi x/L)$. Key nondimensional parameters in this

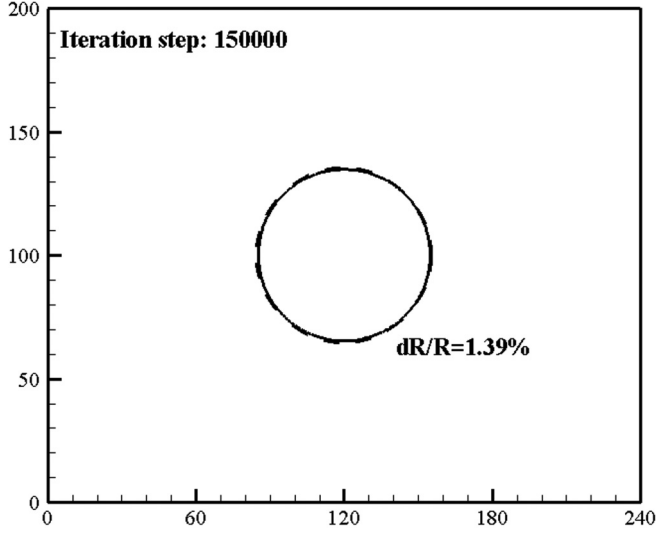


FIG. 4. Mass conservation test in two merging bubbles. The dashed line represents the analytical solution.

problem include the Atwood number $At = (\rho_d - \rho_l)/(\rho_d + \rho_l)$ and the Reynolds number $Re = \rho_d L^{3/2} g^{1/2} / \mu$. In the present paper, the Atwood number is fixed at $At = 0.5$, while two cases with $Re = 256$ and 3000 are simulated using the proposed SMLBM. At this Atwood number, the density ratio of two fluids is 3. In our simulation, three diffuse layers are utilized to ensure smooth transition of density over the interface.

Contours of the order parameter at different moments are presented in Figs. 6 and 7. In these figures, it is observed that the smoothness of the field of the order parameter is well maintained. With the increase of Reynolds number, the interface reveals more severe changes, which are induced by less constraint from the viscous effect. The present results are quite similar to computational results reported in literature [36,37]. The sharpness of the interface is preserved even at a high Reynolds number of $Re = 3000$, which indicates the numerical stability of the method. Quantitative comparisons of interface positions are then carried out in Figs. 8 and 9. The computational results of the present method agree well with reference data in literature [11,38–40], which validates the accuracy of SMLBM in unsteady multiphase flows at high Reynolds number.

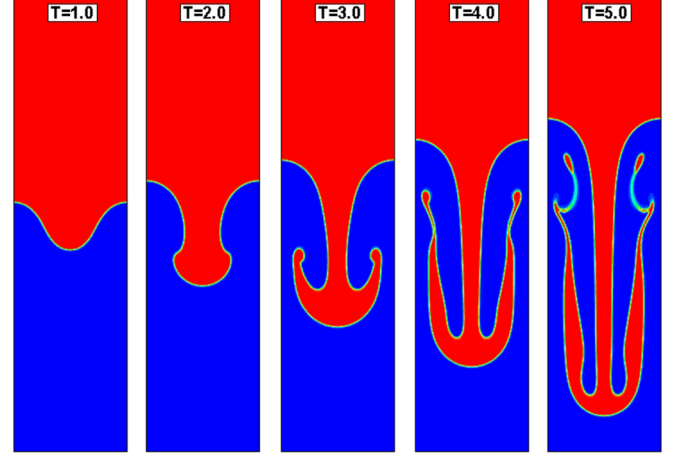


FIG. 6. Contours of the order parameter for Rayleigh-Taylor instability at $At = 0.5$ and $Re = 256$.

D. Bubble rising

Although the above example is an unsteady case with severe interfacial changes, the density ratio is nevertheless small. In this subsection, the example of a bubble rising, which is characterized by a large density ratio and complex interfacial changes, is simulated using the proposed SMLBM for further evaluation of its robustness. The physical configuration of the problem is one bubble of lighter fluid rising in the ambient denser fluid (see Fig. 10 for the initial setup). The rising and the deformation of the bubble are outcomes of the combination effect of buoyance force, surface tension force, and viscous force, which yields three key parameters for this problem: density ratio (ρ_d/ρ_l), Eotvos number ($Eo = \rho_d g D^2 / \sigma$), and Reynolds number ($Re = \rho_d g^{1/2} D^{3/2} / \mu_d$). In our simulation, the density ratio is 1000, which mimics the scenario of an air bubble rising in water. The Reynolds number is fixed at $Re = 35$, and the viscosity ratio is set as $\mu_d/\mu_l = 100$ to maintain consistency with Ref. [41]. The interface thickness is set to be $\xi = 4$.

A mesh independence test is first carried out on the case of $Re = 35$ and $Eo = 125$. Instantaneous interfacial positions obtained by various mesh sizes at a nondimensional time of $T = 4$ are presented in Fig. 11. Few interfacial variations are observed in this figure when the mesh size is finer than 201×401 , which validates the convergence of the proposed

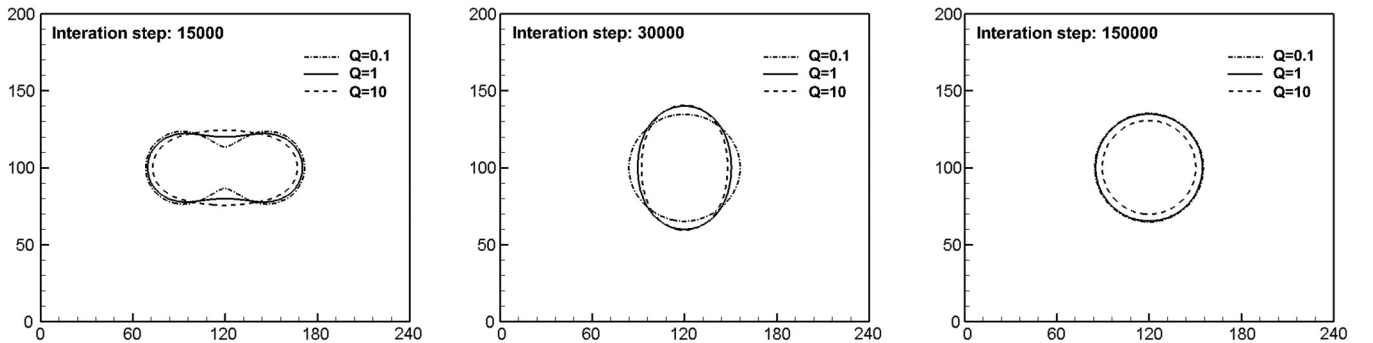


FIG. 5. Interface evolution of two merging bubbles with different diffusion parameters.

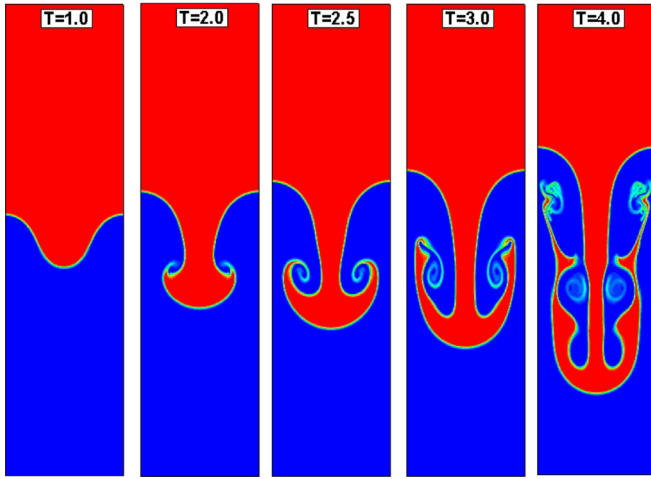


FIG. 7. Contours of the order parameter for Rayleigh-Taylor instability at $At = 0.5$ and $Re = 3000$.

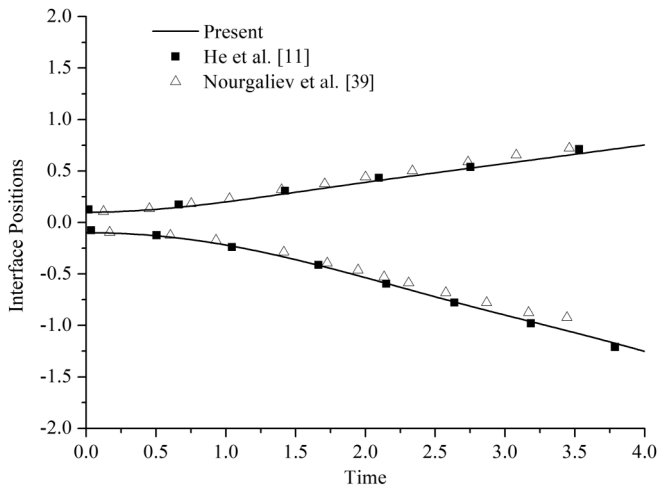


FIG. 8. Time history of interface positions for Rayleigh-Taylor instability at $At = 0.5$ and $Re = 256$.

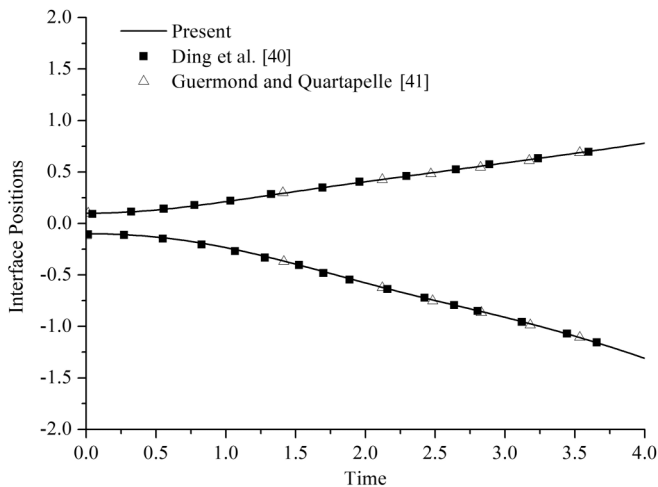


FIG. 9. Time history of interface positions for Rayleigh-Taylor instability at $At = 0.5$ and $Re = 3000$.

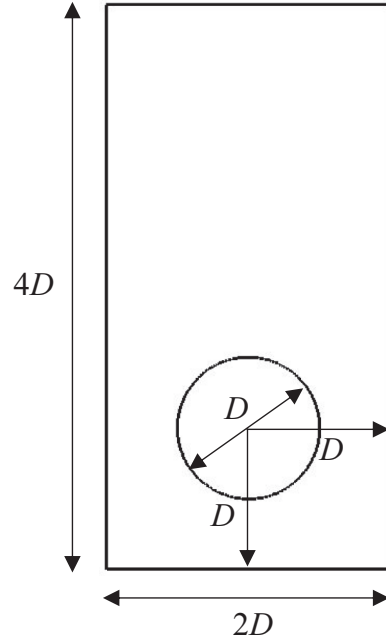


FIG. 10. Illustration of the setup of bubble rising.

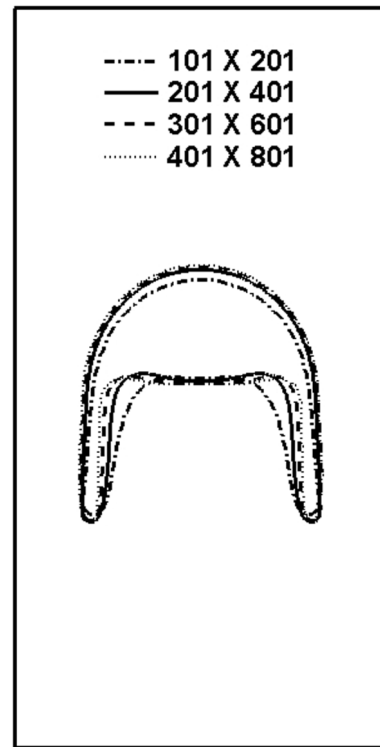
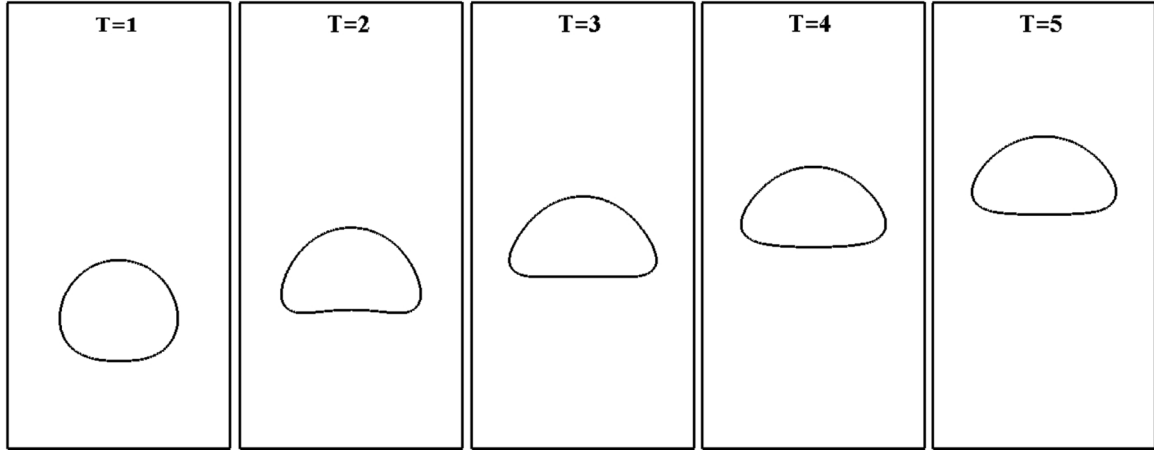


FIG. 11. Instantaneous positions of the interface of the bubble rising at different mesh sizes. $Re = 35$, $Eo = 125$, $T = 4$.

multiphase solver. This validated mesh size will then be utilized in the following cases with $Eo = 10, 50$, and 125 .

Evolutions of the interface are presented in Figs. 12–14. At low Eo number (e.g., $Eo = 10$), the shape of the bubble is constrained by the surface tension force, due to which a semicircle is formed at a later time of rising. With the

FIG. 12. Evolution of the interface for the bubble rising at $Re = 35$ and $Eo = 10$.

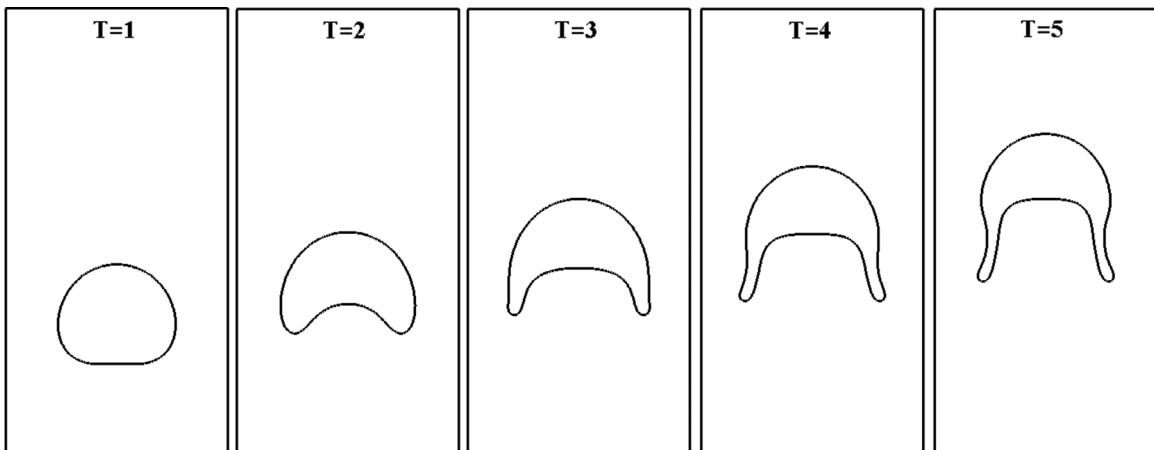
increase of Eo number, the constraint from the surface tension is reduced. Therefore, the deformation of the bubble becomes more severe. This is reflected as the pair of tails formed at a later time of rising. At higher Eo number, the interface exerts lower surface tension force to drag the stretched tails back to the main body, which is reflected as longer tails at the same moment. The contours given by SMLBM are quite similar to the snapshots offered in previous works [41], which suggests that the proposed method can give the correct solution to this problem.

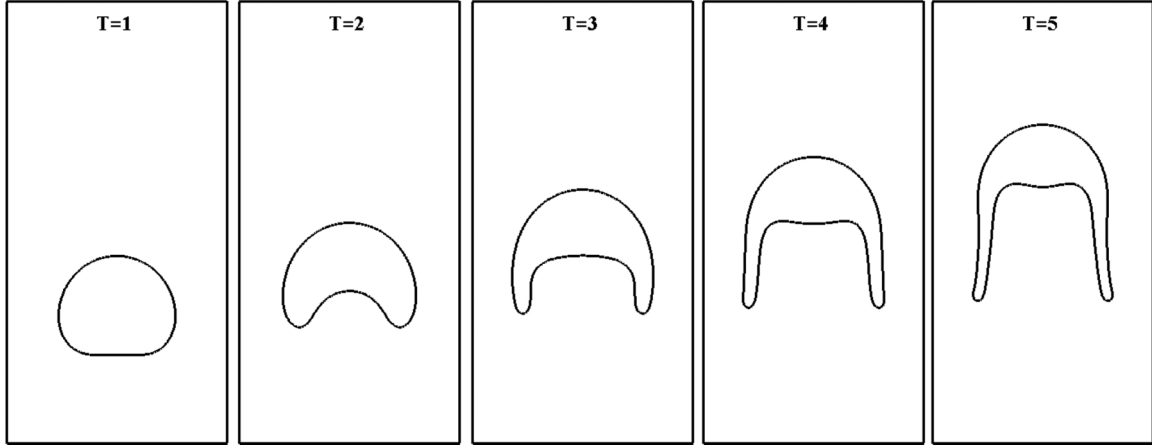
For a more convincing evaluation, quantitative comparison is necessary. Figure 15 gives the time history of the mass center of the rising bubble in the case of $Re = 35$ and $Eo = 125$. The computational results are compared with reference data in literature [30,41]. It can be seen that present results lie within the range of reference data, which validates the accuracy of SMLBM in this problem with large density ratio and complex interface.

E. Droplet splashing on a thin film

Each of the above examples encounters a few difficulties among various challenges of high density ratio, complex

interface, unsteady flow, and high Reynolds number. In the final example, the proposed SMLBM is validated through the problem of a droplet splashing on a thin film in which all these challenges should be properly tackled. The physical setup of the problem is a circular droplet impacting on a thin layer of fluid in the same phase (see Fig. 16). The ambient fluid belongs to a different phase, which preserves distinct physical properties. To model the water droplet in air, the density ratio applied in our simulations is $\rho_d/\rho_l = 1000$. Key nondimensional parameters in this problem include the Reynolds number $Re = 2\rho_d U R/\mu_d$ and the Weber number $We = 2\rho_d U^2 R/\sigma$, and the physical time is nondimensionalized by $2R/U$, where R is the radius of the droplet, U is the initial impact speed, and σ is the surface tension coefficient. As per Lee and Lin's setting [12], dynamic viscosity of the lighter fluid is maintained constant and reveals the viscosity ratio of $\mu_d/\mu_l = 40$ at $Re = 500$. The computational domain is discretized by a uniform mesh size of 2001×501 , in which the radius R is discretized by 100 mesh points. Periodic boundary conditions are implemented on the left and the right boundaries, while no-slip boundary conditions are utilized on the upper and the bottom walls. The interface thickness is set to be $\xi = 5$. The initial impact velocity is $U = 0.01$.

FIG. 13. Evolution of the interface for the bubble rising at $Re = 35$ and $Eo = 50$.

FIG. 14. Evolution of the interface for the bubble rising at $Re = 35$ and $Eo = 125$.

In our simulations, the Weber number is fixed at $We = 8000$, and a series of tests is carried out by varying the Reynolds number from 20 to 8000. As reported in literature, the splashing occurs at higher Reynolds number. Fingers of liquid will form from the end rim of the corona and propagate outward [42,43]. A faster propagation rate of the liquid finger could be physically estimated at higher Reynolds number due to less constraint from the viscous effect. From the numerical perspective, however, instability is likely to emerge in the high Reynolds number scenario, which may hinder the computation from convergence. Therefore, numerical results of this example at Reynolds numbers higher than 1000 are scarce, at least in the LBM community [12,13,44]. For example, in Lee and Lin's work [12], the maximum Reynolds number available at the same mesh spacing ($h = R/100$) is $Re = 500$, as is the case for Shao and Shu's result [13] which incorporates the MRT scheme.

Figures 17–21 present evolutions of interfaces at various Reynolds numbers of $Re = 20, 100, 500, 2000$, and 8000 , respectively. Note that the interfaces in these figures are represented by the contour of $C = 0.5$ and could be regarded as

mean positions of interfaces. It is observed in these results that when the Reynolds number is higher than 100 the splashing phenomenon occurs, which is in accordance with a previous report [12]. In all cases, smooth interface profiles are obtained with no signs of numerical instability. Such performance indicates numerical stability of SMLBM. Specifically, the present method could achieve a stable solution at $Re = 8000$. This challenging case corresponds to the relaxation parameter of $\tau = 0.50075$, which is very much likely to induce numerical instability in conventional LBM.

Figure 22 gives a detailed comparison of interface locations at $T = 2.0$ at various Reynolds numbers. When the Reynolds number is in the moderate range, more stretched fingers could be expected with the increase of Re . At high Reynolds numbers ($Re > 2000$), the shapes of the fingers seem to be not sensitive to the Reynolds number. It could be explained, from the physical perspective, that the inertial effect is overwhelming to the viscous effect at higher Reynolds number. Since the boundary effect has limited influence on the propagation of splashing fingers, the flow patterns at high Reynolds numbers are always similar. Such outcomes are consistent with Josserand and Zaleski's [43] reports that the propagations of the droplet have no significant dependences on the viscosity. It is also suggested that the spread factor $r/2R$ follows the log law [43], which means that the spread factor is proportional to the nondimensional time in log scale, i.e., $r = (2RUt)^{1/2}$. Figure 23 offers the comparison between our computational results and the theoretical prediction. Good agreement can be observed in this figure, which quantitatively validates the accuracy of SMLBM in this problem with various challenges of high density ratio, complex interface, high Reynolds number, and strong impact.

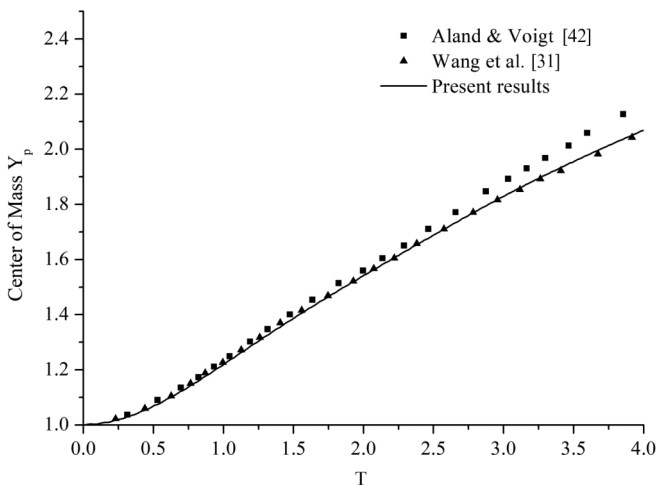
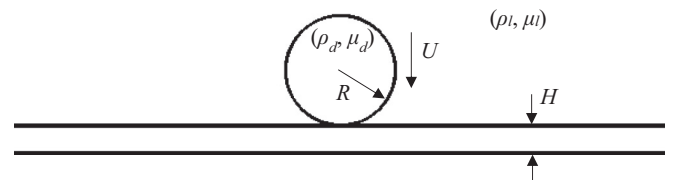
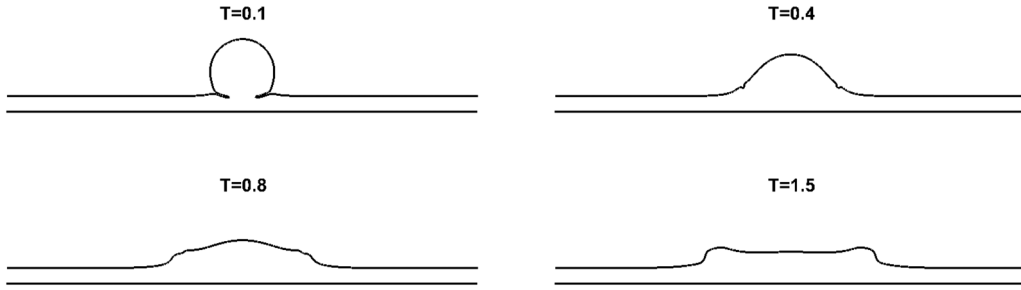
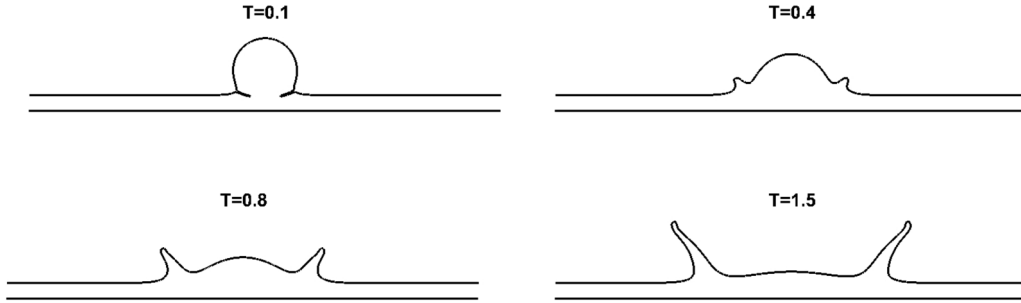
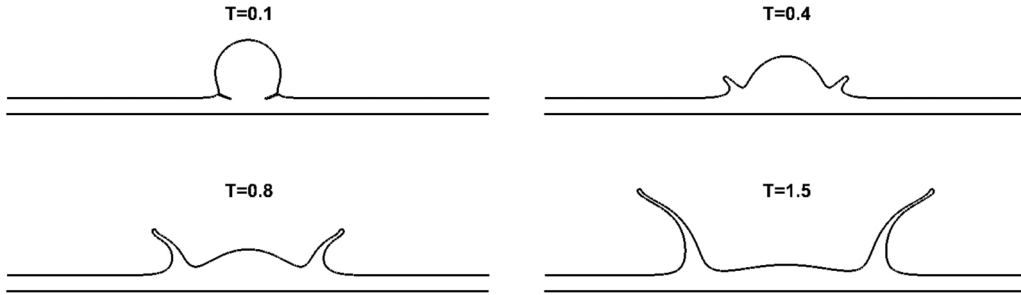
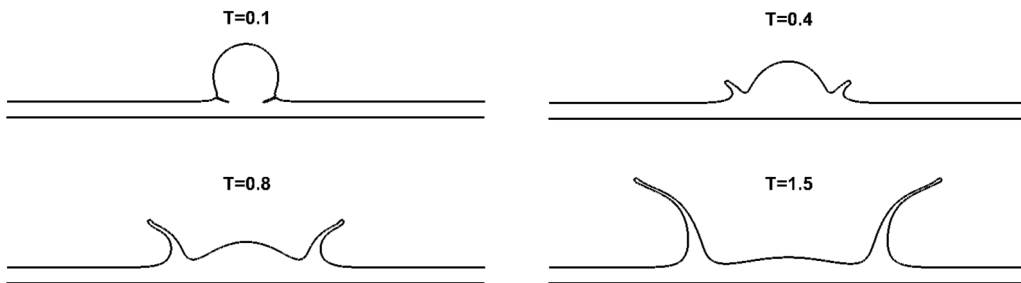
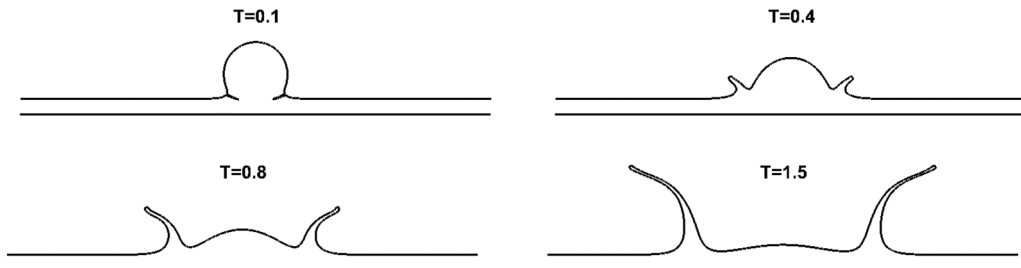
FIG. 15. Time history of the mass center of the rising bubble at $Re = 35$ and $Eo = 125$.

FIG. 16. Schematic diagram of a droplet splashing on a thin film.

FIG. 17. Evolution of a droplet splashing on a thin film at $Re = 20$, $We = 8000$, and $\rho_d/\rho_l = 1000$.FIG. 18. Evolution of a droplet splashing on a thin film at $Re = 100$, $We = 8000$, and $\rho_d/\rho_l = 1000$.FIG. 19. Evolution of a droplet splashing on a thin film at $Re = 500$, $We = 8000$, and $\rho_d/\rho_l = 1000$.FIG. 20. Evolution of a droplet splashing on a thin film at $Re = 2000$, $We = 8000$, and $\rho_d/\rho_l = 1000$.FIG. 21. Evolution of a droplet splashing on a thin film at $Re = 8000$, $We = 8000$, and $\rho_d/\rho_l = 1000$.

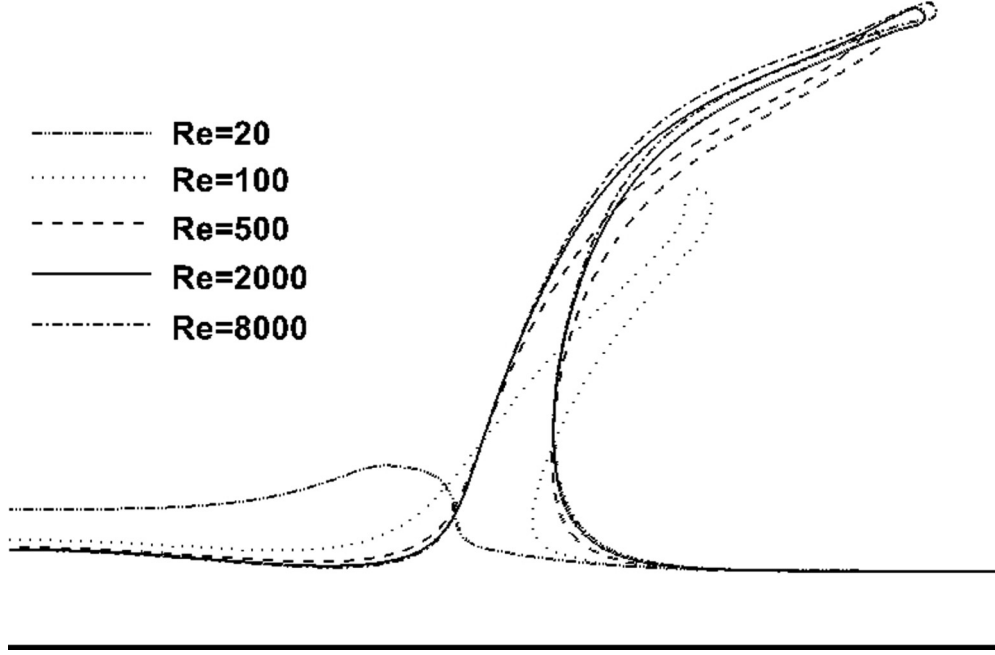


FIG. 22. Interface locations of a droplet splashing on a thin film at $T = 2.0$ at different Reynolds numbers.

V. CONCLUSIONS

A SMLBM is presented in this paper for numerical simulation of incompressible multiphase flows with large density ratios and complex interfaces. This method is developed by reconstructing solutions to macroscopic equations recovered from the multiphase LB model and resolved in a predictor-corrector scheme. SMLBM could eliminate or alleviate drawbacks of LB-based models while maintaining their merits like kinetic nature, simplicity, and explicitness. Unlike previous multiphase LB models, SMLBM directly updates the macroscopic variables instead of distribution functions, which reduces memory cost and facilitates implementation of physical

boundary conditions. It is also expected that SMLBM could inherit the numerical stability of its precursor, simplified lattice Boltzmann method, which is developed for single phase incompressible flows and could be theoretically proven to be stable at high Reynolds numbers.

Validation of SMLBM is performed through a series of representative numerical examples including Laplace's law, two merging bubbles, Rayleigh-Taylor instability, a bubble rising, and a droplet splashing on a thin film. Various numerical challenges like large density ratios (up to 1000), complex interfaces, and high Reynolds numbers (up to 8000 in the example of a droplet splashing on a thin film) are encountered in these examples. It is observed in numerical tests that SMLBM could properly tackle these difficulties and give accurate and stable solutions. These outcomes indicate that the present SMLBM is a promising solver in the field of multiphase simulation.

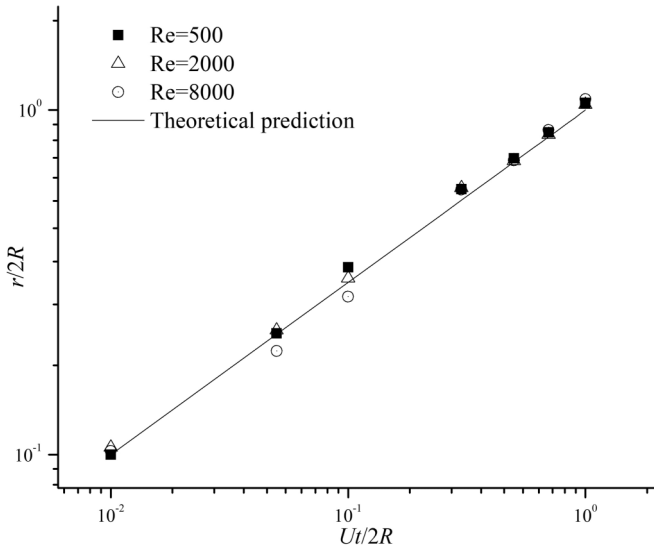


FIG. 23. Spread factor ($r/2R$) as a function of nondimensional time ($Ut/2R$) in log scale.

APPENDIX: CHAPMAN-ENKSOG EXPANSION ANALYSIS OF THE MULTIPHASE LATTICE BOLTZMANN MODEL AND THE CAHN-HILLIARD MODEL

The multiphase lattice Boltzmann model and the Cahn-Hilliard model in the LB framework are

$$f_{\alpha}(\mathbf{r} + \mathbf{e}_{\alpha}\delta_t, t + \delta_t) = f_{\alpha}(\mathbf{r}, t) - \frac{f_{\alpha}(\mathbf{r}, t) - f_{\alpha}^{\text{eq}}(\mathbf{r}, t)}{\tau} + H_{\alpha}, \quad (\text{A1})$$

$$g_{\alpha}(\mathbf{r} + \mathbf{e}_{\alpha}\delta_t, t + \delta_t) = g_{\alpha}(\mathbf{r}, t) - \frac{g_{\alpha}(\mathbf{r}, t) - g_{\alpha}^{\text{eq}}(\mathbf{r}, t)}{\tau_c} \quad (\text{A2})$$

where variables are defined in Eqs. (2)–(5) and (15).

To perform C-E analysis on the above models, the distribution functions, space and time derivatives, and forcing terms can be expanded in multiple scales as

$$f_\alpha = f_\alpha^{(0)} + \varepsilon f_\alpha^{(1)} + \varepsilon^2 f_\alpha^{(2)}, \quad g_\alpha = g_\alpha^{(0)} + \varepsilon g_\alpha^{(1)} + \varepsilon^2 g_\alpha^{(2)}, \quad \partial_t = \varepsilon \partial_{t_0} + \varepsilon^2 \partial_{t_1}, \quad \nabla = \varepsilon \nabla_1, \quad H_\alpha = \varepsilon H_\alpha^{(1)}. \quad (\text{A3})$$

Substituting Eq. (A3) into Eqs. (A1) and (A2) gives

$$\begin{aligned} & \left(\varepsilon \frac{\partial}{\partial t_0} + \varepsilon^2 \frac{\partial}{\partial t_1} + \varepsilon \mathbf{e}_\alpha \cdot \nabla_1 \right) (f_\alpha^{(0)} + \varepsilon f_\alpha^{(1)} + \varepsilon^2 f_\alpha^{(2)}) + \frac{\delta_t}{2} \left(\varepsilon \frac{\partial}{\partial t_0} + \varepsilon^2 \frac{\partial}{\partial t_1} + \varepsilon \mathbf{e}_\alpha \cdot \nabla_1 \right)^2 (f_\alpha^{(0)} + \varepsilon f_\alpha^{(1)} + \varepsilon^2 f_\alpha^{(2)}) \\ &= -\frac{1}{\tau \delta_t} (f_\alpha^{(0)} + \varepsilon f_\alpha^{(1)} + \varepsilon^2 f_\alpha^{(2)} - f_\alpha^{\text{eq}}) + \varepsilon H_\alpha^{(1)}, \end{aligned} \quad (\text{A4})$$

$$\begin{aligned} & \left(\varepsilon \frac{\partial}{\partial t_0} + \varepsilon^2 \frac{\partial}{\partial t_1} + \varepsilon \mathbf{e}_\alpha \cdot \nabla_1 \right) (g_\alpha^{(0)} + \varepsilon g_\alpha^{(1)} + \varepsilon^2 g_\alpha^{(2)}) + \frac{\delta_t}{2} \left(\varepsilon \frac{\partial}{\partial t_0} + \varepsilon^2 \frac{\partial}{\partial t_1} + \varepsilon \mathbf{e}_\alpha \cdot \nabla_1 \right)^2 (g_\alpha^{(0)} + \varepsilon g_\alpha^{(1)} + \varepsilon^2 g_\alpha^{(2)}) \\ &= -\frac{1}{\tau_C \delta_t} (g_\alpha^{(0)} + \varepsilon g_\alpha^{(1)} + \varepsilon^2 g_\alpha^{(2)} - g_\alpha^{\text{eq}}). \end{aligned} \quad (\text{A5})$$

From the above equation, the following relationships can be established in different scales:

$$\varepsilon^0 : f_\alpha^{(0)} = f_\alpha^{\text{eq}}, \quad (\text{A6})$$

$$\varepsilon^1 : \frac{\partial}{\partial t_0} f_\alpha^{(0)} + \mathbf{e}_\alpha \cdot \nabla_1 f_\alpha^{(0)} = -\frac{1}{\tau \delta_t} f_\alpha^{(1)} + H_\alpha^{(1)}, \quad (\text{A7})$$

$$\varepsilon^2 : \frac{\partial}{\partial t_1} f_\alpha^{(0)} + \frac{\partial}{\partial t_0} \left(1 - \frac{1}{2\tau} \right) f_\alpha^{(1)} + \mathbf{e}_\alpha \cdot \nabla_1 \left(1 - \frac{1}{2\tau} \right) f_\alpha^{(1)} = -\frac{1}{\tau \delta_t} f_\alpha^{(2)} - \frac{\delta_t}{2} \left(\frac{\partial}{\partial t_0} + \mathbf{e}_\alpha \cdot \nabla_1 \right) H_\alpha^{(1)}, \quad (\text{A8})$$

$$\varepsilon^0 : g_\alpha^{(0)} = g_\alpha^{\text{eq}}, \quad (\text{A9})$$

$$\varepsilon^1 : \frac{\partial}{\partial t_0} g_\alpha^{(0)} + \mathbf{e}_\alpha \cdot \nabla_1 g_\alpha^{(0)} = -\frac{1}{\tau_C \delta_t} g_\alpha^{(1)}, \quad (\text{A10})$$

$$\varepsilon^2 : \frac{\partial}{\partial t_1} g_\alpha^{(0)} + \frac{\partial}{\partial t_0} \left(1 - \frac{1}{2\tau_C} \right) g_\alpha^{(1)} + \mathbf{e}_\alpha \cdot \nabla_1 \left(1 - \frac{1}{2\tau_C} \right) g_\alpha^{(1)} = -\frac{1}{\tau_C \delta_t} g_\alpha^{(2)}, \quad (\text{A11})$$

and the following relationships are established [26]:

$$\sum_\alpha f_\alpha^{(1)} = \frac{1}{2} \mathbf{u} \cdot \nabla_1 \psi(\rho) \delta_t, \quad \sum_\alpha \mathbf{e}_\alpha f_\alpha^{(1)} = -\frac{c_s^2}{2} (\mathbf{F}_s + \mathbf{G})_1 \delta_t, \quad (\text{A12})$$

$$\sum_\alpha f_\alpha^{(2)} = \sum_\alpha \mathbf{e}_\alpha f_\alpha^{(2)} = 0, \quad (\text{A13})$$

$$\sum_\alpha H_\alpha = -\left(1 - \frac{1}{2\tau} \right) \mathbf{u} \cdot \nabla \psi(\rho), \quad \sum_\alpha \mathbf{e}_\alpha H_\alpha = \left(1 - \frac{1}{2\tau} \right) c_s^2 (\mathbf{F}_s + \mathbf{G}). \quad (\text{A14})$$

From Eqs. (A7) and (A10) the nonequilibrium parts are expressed as

$$\varepsilon f_\alpha^{(1)} = -\tau \delta_t D f_\alpha^{\text{eq}} + \tau \delta_t H_\alpha, \quad (\text{A15})$$

$$\varepsilon g_\alpha^{(1)} = -\tau_C \delta_t D g_\alpha^{\text{eq}}. \quad (\text{A16})$$

To reveal the equivalent macroscopic equations, we need to consider various moments of the expanded formulations and combine them in the macroscopic scale. Zeroth moments of Eqs. (A7), (A8), (A10), and (A11) give, respectively,

$$\frac{\partial}{\partial t_0} \sum_\alpha f_\alpha^{(0)} + \nabla_1 \cdot \sum_\alpha \mathbf{e}_\alpha f_\alpha^{(0)} = -\frac{1}{\tau \delta_t} \sum_\alpha f_\alpha^{(1)} + \sum_\alpha H_\alpha^{(1)} \Rightarrow \frac{\partial p}{\partial t_0} + \nabla_1 \cdot \sum_\alpha \mathbf{e}_\alpha f_\alpha^{(0)} = \mathbf{u} \cdot \nabla_1 \rho c_s^2, \quad (\text{A17})$$

$$\begin{aligned} & \frac{\partial}{\partial t_1} \sum_\alpha f_\alpha^{(0)} + \frac{\partial}{\partial t_0} \left(1 - \frac{1}{2\tau} \right) \sum_\alpha f_\alpha^{(1)} + \nabla_1 \cdot \left(1 - \frac{1}{2\tau} \right) \sum_\alpha \mathbf{e}_\alpha f_\alpha^{(1)} \\ &= -\frac{1}{\tau \delta_t} \sum_\alpha f_\alpha^{(2)} - \frac{\delta_t}{2} \left(\frac{\partial}{\partial t_0} + \mathbf{e}_\alpha \cdot \nabla_1 \right) \sum_\alpha H_\alpha^{(1)} \Rightarrow \frac{\partial p}{\partial t_1} = 0, \end{aligned} \quad (\text{A18})$$

$$\frac{\partial}{\partial t_0} \sum_\alpha g_\alpha^{(0)} + \nabla_1 \cdot \sum_\alpha \mathbf{e}_\alpha g_\alpha^{(0)} = 0 \Rightarrow \frac{\partial C}{\partial t_0} + \nabla_1 \cdot \sum_\alpha \mathbf{e}_\alpha g_\alpha^{\text{eq}} = 0, \quad (\text{A19})$$

$$\begin{aligned} \frac{\partial}{\partial t_1} \sum_{\alpha} g_{\alpha}^{(0)} + \frac{\partial}{\partial t_0} \left(1 - \frac{1}{2\tau}\right) \sum_{\alpha} g_{\alpha}^{(1)} + \nabla_1 \cdot \left(1 - \frac{1}{2\tau}\right) \sum_{\alpha} \mathbf{e}_{\alpha} g_{\alpha}^{(1)} \\ = -\frac{1}{\tau \delta_t} \sum_{\alpha} g_{\alpha}^{(2)} \Rightarrow \frac{\partial C}{\partial t_1} + \nabla_1 \cdot \left(\frac{1}{2} - \tau\right) \delta_t \sum_{\alpha} \mathbf{e}_{\alpha} D_1 g_{\alpha}^{\text{eq}} = 0. \end{aligned} \quad (\text{A20})$$

Combining Eqs. (A17) and (A18) leads to the continuity equation:

$$\frac{\partial p}{\partial t} + \nabla \cdot \sum_{\alpha} \mathbf{e}_{\alpha} f_{\alpha}^{\text{eq}} = \mathbf{u} \cdot \nabla \rho c_s^2. \quad (\text{A21})$$

Consolidating Eqs. (A19) and (A20) to the same scale yields the Cahn-Hilliard equation:

$$\frac{\partial C}{\partial t} + \nabla \cdot \sum_{\alpha} \mathbf{e}_{\alpha} g_{\alpha}^{\text{eq}} + \nabla \cdot \left(\frac{1}{2} - \tau\right) \delta_t \sum_{\alpha} \mathbf{e}_{\alpha} D g_{\alpha}^{\text{eq}} = 0. \quad (\text{A22})$$

To recover the momentum equation, consider the first moments of Eqs. (A7) and (A8):

$$\begin{aligned} \frac{\partial}{\partial t_0} \sum_{\alpha} \mathbf{e}_{\alpha} f_{\alpha}^{(0)} + \nabla_1 \cdot \sum_{\alpha} (\mathbf{e}_{\alpha})_j (\mathbf{e}_{\alpha})_k f_{\alpha}^{(0)} = -\frac{1}{\tau \delta_t} \sum_{\alpha} \mathbf{e}_{\alpha} f_{\alpha}^{(1)} + \sum_{\alpha} \mathbf{e}_{\alpha} H_{\alpha}^{(1)} \Rightarrow \frac{\partial \rho \mathbf{u} c_s^2}{\partial t_0} + \nabla_1 \cdot \sum_{\alpha} (\mathbf{e}_{\alpha})_j (\mathbf{e}_{\alpha})_k f_{\alpha}^{(0)} = c_s^2 (\mathbf{F}_s + \mathbf{G})_1, \end{aligned} \quad (\text{A23})$$

$$\begin{aligned} \frac{\partial}{\partial t_1} \sum_{\alpha} \mathbf{e}_{\alpha} f_{\alpha}^{(0)} + \frac{\partial}{\partial t_0} \left(1 - \frac{1}{2\tau}\right) \sum_{\alpha} \mathbf{e}_{\alpha} f_{\alpha}^{(1)} + \nabla_1 \cdot \left(1 - \frac{1}{2\tau}\right) \sum_{\alpha} (\mathbf{e}_{\alpha})_j (\mathbf{e}_{\alpha})_k f_{\alpha}^{(1)} \\ = -\frac{1}{\tau \delta_t} \sum_{\alpha} \mathbf{e}_{\alpha} f_{\alpha}^{(2)} - \frac{\delta_t}{2} \left(\frac{\partial}{\partial t_0} \sum_{\alpha} \mathbf{e}_{\alpha} H_{\alpha}^{(1)} + \nabla_1 \sum_{\alpha} (\mathbf{e}_{\alpha})_j (\mathbf{e}_{\alpha})_k H_{\alpha}^{(1)} \right) \Rightarrow \frac{\partial \rho \mathbf{u} c_s^2}{\partial t_1} + \nabla_1 \cdot \left(1 - \frac{1}{2\tau}\right) \sum_{\alpha} (\mathbf{e}_{\alpha})_j (\mathbf{e}_{\alpha})_k f_{\alpha}^{(1)} \\ = -\frac{\delta_t}{2} \nabla_1 \sum_{\alpha} (\mathbf{e}_{\alpha})_j (\mathbf{e}_{\alpha})_k H_{\alpha}^{(1)}. \end{aligned} \quad (\text{A24})$$

Combining Eqs. (A23) and (A24) yields

$$\frac{\partial \rho \mathbf{u} c_s^2}{\partial t} + \nabla \cdot \sum_{\alpha} (\mathbf{e}_{\alpha})_j (\mathbf{e}_{\alpha})_k \left[f_{\alpha}^{\text{eq}} + \left(1 - \frac{1}{2\tau}\right) \varepsilon f_{\alpha}^{(1)} \right] + \frac{\delta_t}{2} \nabla \sum_{\alpha} (\mathbf{e}_{\alpha})_j (\mathbf{e}_{\alpha})_k H_{\alpha} = c_s^2 (\mathbf{F}_s + \mathbf{G}). \quad (\text{A25})$$

Substituting the formula of the nonequilibrium term [Eq. (A15)], the above equation can be simplified into the following momentum equation:

$$\frac{\partial \rho \mathbf{u} c_s^2}{\partial t} + \nabla \cdot \sum_{\alpha} (\mathbf{e}_{\alpha})_j (\mathbf{e}_{\alpha})_k \left[f_{\alpha}^{\text{eq}} - \left(\tau - \frac{1}{2}\right) \delta_t D f_{\alpha}^{\text{eq}} \right] + \nabla \tau \delta_t \sum_{\alpha} (\mathbf{e}_{\alpha})_j (\mathbf{e}_{\alpha})_k H_{\alpha} = c_s^2 (\mathbf{F}_s + \mathbf{G}). \quad (\text{A26})$$

-
- [1] C. W. Hirt and B. D. Nichols, Volume of fluid (VOF) method for the dynamics of free boundaries, *J. Comput. Phys.* **39**, 201 (1981).
 - [2] M. Sussman, P. Smereka, and S. Osher, A level set approach for computing solutions to incompressible two-phase flow, *J. Comput. Phys.* **114**, 146 (1994).
 - [3] S. O. Unverdi and G. Tryggvason, A front-tracking method for viscous, incompressible, multi-fluid flows, *J. Comput. Phys.* **100**, 25 (1992).
 - [4] D. M. Anderson, G. B. McFadden, and A. A. Wheeler, Diffuse-interface methods in fluid mechanics, *Annu. Rev. Fluid Mech.* **30**, 139 (1998).
 - [5] S. Chen and G. D. Doolen, Lattice Boltzmann method for fluid flows, *Annu. Rev. Fluid Mech.* **30**, 329 (1998).
 - [6] C. K. Aidun and J. R. Clausen, Lattice-Boltzmann method for complex flows, *Annu. Rev. Fluid Mech.* **42**, 439 (2010).
 - [7] R. Benzi, S. Succi, and M. Vergassola, The lattice Boltzmann equation: Theory and applications, *Phys. Rep.* **222**, 145 (1992).
 - [8] A. K. Gunstensen, D. H. Rothman, S. Zaleski, and G. Zanetti, Lattice Boltzmann model of immiscible fluids, *Phys. Rev. A* **43**, 4320 (1991).
 - [9] X. Shan and H. Chen, Lattice Boltzmann model for simulating flows with multiple phases and components, *Phys. Rev. E* **47**, 1815 (1993).
 - [10] M. R. Swift, E. Orlandini, W. Osborn, and J. Yeomans, Lattice Boltzmann simulations of liquid-gas and binary fluid systems, *Phys. Rev. E* **54**, 5041 (1996).
 - [11] X. He, S. Chen, and R. Zhang, A lattice Boltzmann scheme for incompressible multiphase flow and its application in simulation of Rayleigh-Taylor instability, *J. Comput. Phys.* **152**, 642 (1999).

- [12] T. Lee and C.-L. Lin, A stable discretization of the lattice Boltzmann equation for simulation of incompressible two-phase flows at high density ratio, *J. Comput. Phys.* **206**, 16 (2005).
- [13] J. Shao and C. Shu, A hybrid phase field multiple relaxation time lattice Boltzmann method for the incompressible multiphase flow with large density contrast, *Int. J. Numer. Methods Fluids* **77**, 526 (2015).
- [14] R. H. H. Abadi, M. H. Rahimian, and A. Fakhari, Conservative phase-field lattice-Boltzmann model for ternary fluids, *J. Comput. Phys.* **374**, 668 (2018).
- [15] B. Wei, H. Huang, J. Hou, and M. C. Sukop, Study on the meniscus-induced motion of droplets and bubbles by a three-phase Lattice Boltzmann model, *Chem. Eng. Sci.* **176**, 35 (2018).
- [16] M. Wöhrwag, C. Semperebon, A. M. Moqaddam, I. Karlin, and H. Kusumaatmaja, Ternary Free-Energy Entropic Lattice Boltzmann Model with a High Density Ratio, *Phys. Rev. Lett.* **120**, 234501 (2018).
- [17] Z. Guo and C. Shu, *Lattice Boltzmann Method and its Applications in Engineering* (World Scientific, Singapore, 2013).
- [18] D. d'Humières, Multiple-relaxation-time lattice Boltzmann models in three dimensions, *Phil. Trans. R. Soc. A* **360**, 437 (2002).
- [19] Z. Guo, C. Zheng, and B. Shi, An extrapolation method for boundary conditions in lattice Boltzmann method, *Phys. Fluids* **14**, 2007 (2002).
- [20] J. D. Sterling and S. Chen, Stability analysis of lattice Boltzmann methods, *J. Comput. Phys.* **123**, 196 (1996).
- [21] A. Fakhari and T. Lee, Multiple-relaxation-time lattice Boltzmann method for immiscible fluids at high Reynolds numbers, *Phys. Rev. E* **87**, 023304 (2013).
- [22] K. N. Premnath and J. Abraham, Three-dimensional multi-relaxation time (MRT) lattice-Boltzmann models for multiphase flow, *J. Comput. Phys.* **224**, 539 (2007).
- [23] S. Chikatamarla and I. Karlin, Entropic Lattice Boltzmann Method for Multiphase Flows, *Phys. Rev. Lett.* **114**, 174502 (2015).
- [24] Z. Chen, C. Shu, Y. Wang, L. M. Yang, and D. Tan, A simplified lattice Boltzmann method without evolution of distribution function, *Adv. Appl. Math. Mech.* **9**, 1 (2017).
- [25] Z. Chen, C. Shu, D. Tan, and C. Wu, On improvements of simplified and highly stable lattice Boltzmann method: Formulations, boundary treatment, and stability analysis, *Int. J. Numer. Methods Fluids* **87**, 161 (2018).
- [26] J. Shao, C. Shu, H. Huang, and Y. Chew, Free-energy-based lattice Boltzmann model for the simulation of multiphase flows with density contrast, *Phys. Rev. E* **89**, 033309 (2014).
- [27] Y. Qian, D. d'Humières, and P. Lallemand, Lattice BGK models for Navier-Stokes equation, *Europhys. Lett.* **17**, 479 (1992).
- [28] M. Geier, A. Fakhari, and T. Lee, Conservative phase-field lattice Boltzmann model for interface tracking equation, *Phys. Rev. E* **91**, 063309 (2015).
- [29] F. Ren, B. Song, M. C. Sukop, and H. Hu, Improved lattice Boltzmann modeling of binary flow based on the conservative Allen-Cahn equation, *Phys. Rev. E* **94**, 023311 (2016).
- [30] Y. Wang, C. Shu, J. Shao, J. Wu, and X. Niu, A mass-conserved diffuse interface method and its application for incompressible multiphase flows with large density ratio, *J. Comput. Phys.* **290**, 336 (2015).
- [31] H. Zheng, C. Shu, and Y.-T. Chew, A lattice Boltzmann model for multiphase flows with large density ratio, *J. Comput. Phys.* **218**, 353 (2006).
- [32] J. Huang, C. Shu, and Y. Chew, Mobility-dependent bifurcations in capillarity-driven two-phase fluid systems by using a lattice Boltzmann phase-field model, *Int. J. Numer. Methods Fluids* **60**, 203 (2009).
- [33] J. Kim and P. Moin, Application of a fractional-step method to incompressible Navier-Stokes equations, *J. Comput. Phys.* **59**, 308 (1985).
- [34] C. Shu, Y. Wang, C. Teo, and J. Wu, Development of lattice Boltzmann flux solver for simulation of incompressible flows, *Adv. Appl. Math. Mech.* **6**, 436 (2014).
- [35] H. Wang, Z. Chai, B. Shi, and H. Liang, Comparative study of the lattice Boltzmann models for Allen-Cahn and Cahn-Hilliard equations, *Phys. Rev. E* **94**, 033304 (2016).
- [36] Y. Wang, C. Shu, H. Huang, and C. Teo, Multiphase lattice Boltzmann flux solver for incompressible multiphase flows with large density ratio, *J. Comput. Phys.* **280**, 404 (2015).
- [37] G. Tryggvason, Numerical simulations of the Rayleigh-Taylor instability, *J. Comput. Phys.* **75**, 253 (1988).
- [38] R. Nourgaliev, T.-N. Dinh, and T. Theofanous, A pseudocompressibility method for the numerical simulation of incompressible multifluid flows, *Int. J. Multiphase Flow* **30**, 901 (2004).
- [39] H. Ding, P. D. Speltz, and C. Shu, Diffuse interface model for incompressible two-phase flows with large density ratios, *J. Comput. Phys.* **226**, 2078 (2007).
- [40] J.-L. Guermond and L. Quartapelle, A projection FEM for variable density incompressible flows, *J. Comput. Phys.* **165**, 167 (2000).
- [41] S. Aland and A. Voigt, Benchmark computations of diffuse interface models for two-dimensional bubble dynamics, *Int. J. Numer. Methods Fluids* **69**, 747 (2012).
- [42] D. A. Weiss and A. L. Yarin, Single drop impact onto liquid films: Neck distortion, jetting, tiny bubble entrainment, and crown formation, *J. Fluid Mech.* **385**, 229 (1999).
- [43] C. Josserand and S. Zaleski, Droplet splashing on a thin liquid film, *Phys. Fluids* **15**, 1650 (2003).
- [44] Q. Li, K. Luo, and X. Li, Lattice Boltzmann modeling of multiphase flows at large density ratio with an improved pseudopotential model, *Phys. Rev. E* **87**, 053301 (2013).